Advanced Healthcare Materials

ADVANCED HEALTHCARE MATERIALS
www.advhealthmat.de

RESEARCH ARTICLE OPEN ACCESS

Genipin-Crosslinked, Silane-Anchored 3D Tumor–Stroma Microtissues for High-Content On-Chip Drug Testing

Doriane Le Manach[1] | Reza Kowsari-Esfahan[2] | Emilia Reszczyńska[1,3] | Philippe Nghe[2] | Matthias Nees[1,4]

[1]Department of Biochemistry and Molecular Biology, Medical University of Lublin, Lublin, Poland | [2]Laboratoire De Biophysique et Evolution, UMR CNRS-ESPCI 8231 Chimie Biologie Innovation, PSL University, Paris, France | [3]Department of Plant Physiology and Biophysics, Institute of Biological Sciences, Faculty of Biology and Biotechnology, Maria Curie-Skłodowska University, Lublin, Poland | [4]FICAN West Cancer Centre Laboratory, Cancer Research Unit, Institute of Biomedicine, Turku University Hospital, University of Turku, Turku, Finland

Correspondence: Doriane Le Manach (doriane.le-manach@umlub.pl) | Matthias Nees (matthias.nees@umlub.edu.pl)

Received: 18 July 2025 | **Revised:** 1 April 2026 | **Accepted:** 29 April 2026

Keywords: 3D tumor-fibroblast co-culture | extracellular matrix stabilization | Genipin crosslinking | high-content imaging | in vitro chemosensitivity assays | semi-automated segmentation | silane-functionalization microfluidic devices

ABSTRACT

Physiologically relevant 3D tumor models incorporating extracellular matrix (ECM) and cancer-associated fibroblasts (CAFs) are essential for studying tumor progression and drug resistance, yet often suffer from hydrogel contraction and instability—especially in microfluidic formats, where ECM deformation hampers long-term culture and quantitative imaging. Here, we present a microfluidic tumor–fibroblast co-culture platform for head and neck squamous cell carcinoma (HNSCC) that overcomes these limitations via a dual strategy: APTES-mediated surface silanization anchors the ECM to the chip, combined with Genipin-based crosslinking, which modestly increases hydrogel stiffness and progressively reinforces the network without compromising cell viability, as confirmed by time- and frequency-resolved rheology. Fourier-transform infrared spectroscopy (FTIR) verified successful collagen crosslinking while preserving reactive —OH and —NH_2 groups, enabling covalent bonding to the APTES-functionalized chip. The platform further integrates semi-automated segmentation and high-content imaging to quantify dynamic phenotypic drug responses at both single-cell and multicellular/tissue organization levels. Drug chemosensitivity assays, including co-culture with patient-derived CAFs, enabled quantitative assessment of clinically relevant chemoprotective effects. By combining biomaterial engineering with functional microfluidic design, this system enables reproducible, physiologically relevant modeling of tumor–fibroblast interactions, offering a scalable tool for preclinical drug chemosensitivity screening and clinical translation.

1 | Introduction

Head and neck cancer (HNC) is the seventh most common cancer globally, with head and neck squamous cell carcinoma (HNSCC) accounting for the majority of cases, while other subtypes, such as adenocarcinomas, are much less frequent [1]. Despite recent improvements in surgery, chemotherapy, and radiotherapy, the 5-year survival rate for HNSCC remains close to 50%, largely due to late diagnosis, aggressive tumor biology, and limited efficacy of current treatments [2, 3]. Although immunotherapies have marked significant improvements in patient outcomes, their benefits are limited to only a subset of patients, posing economic and clinical challenges [4]. This underscores an urgent need for more effective, accessible therapies, including pathway-specific small-molecule inhibitors, personalized combination treatments, and predictive, physiologically relevant drug-screening platforms for advanced and metastatic disease.

A key bottleneck in developing such therapies is the inadequacy of existing preclinical models. Traditional two-dimensional (2D) cell cultures and long-established tumor cell lines, adapted to artificial plastic substrates, lack the complex heterogeneity, spatial architecture, and microenvironmental cues that define primary tumors. Similarly, preclinical animal models, such as mouse xenografts and patient-derived xenografts (PDOs), fall short in replicating the native human tumor microenvironment (TME) [5, 6]. These models are often highly reductionist and fail to accurately predict clinical drug responses, resulting in costly late-stage failures in drug development.

Tumor heterogeneity adds another layer of complexity, with both genetic and non-genetic cellular diversity observed between patients and within individual tumors. This high level of tumor cell heterogeneity increases during tumor progression and contributes to therapy resistance, metastasis, and relapse [6]. To better represent this biological diversity, we use early-passage tumor cell lines and patient-derived cancer-associated fibroblasts (CAFs) established directly from fresh biopsies. For example, early-passage cell lines established from primary HNSCC biopsies preserve heterogeneity, differentiation potential, and the physiological relevance of head and neck cancer cells, unlike long-term-cultured lines that show massive genetic drift over time [7].

Critical components of the original TME—extracellular matrix (ECM), fibroblasts, immune cells, and endothelial cells—are typically absent in 2D cultures, limiting their ability to recapitulate tumor complexity and dynamic cellular crosstalk [8–10]. Recent technological advances, including single-cell RNA sequencing and spatial proteomics, have revealed previously unrecognized stromal heterogeneity, identifying multiple CAF subtypes with distinct roles in tumor progression [11–13]. Diverse CAFs secrete growth factors, cytokines, chemokines, and extracellular vesicles that drive immune evasion, epithelial-to-mesenchymal transition (EMT), tumor cell invasion and metastasis, therapy resistance, and ECM remodeling—contributing to tumor stiffness, fibrosis, and desmoplasia [14, 15]. Faithful incorporation of CAFs and tumor-specific ECM is thus critical for physiologically relevant models that more faithfully replicate the in vivo tumor architecture and potentially predict therapeutic outcomes. Collagen type I (COL), a major ECM component in solid tumors, enhances the physiological relevance of 3D culture systems through its biocompatibility, defined chemical composition, and ability to support integrin-mediated adhesion, migration, and invasion of tumor cells and fibroblasts [16–18].

However, COL-based hydrogels also introduce significant technical challenges: fibroblasts and invasive tumor cells actively remodel the COL-rich ECM and exert traction forces that deform, contract, and potentially disintegrate the hydrogel scaffold [19–21]. While this dynamic remodeling partially mimics fibrosis and desmoplasia, important features of aggressive tumors observed in vivo, it also undermines the structural and mechanical stability, reproducibility, and cell viability of the in vitro models—especially limiting their application for high-throughput drug screening and long-term assays [22, 23].

To overcome these limitations, we developed a microfluidic platform (microphysiological system) that stabilizes ex vivo tumor microtissues within a crosslinked hydrogel matrix covalently anchored to the device surface. Our approach combines Genipin as a crosslinking agent for a composite ECM hydrogel based on COL, hyaluronic acid (HA), and Matrigel, with silane-based APTES surface functionalization of PDMS/glass microfluidic chips. This integrated (bio)materials strategy enhances matrix structural and mechanical integrity and adhesion, thus effectively preventing contraction and preserving the 3D architecture of co-cultures containing patient-derived CAFs and HNSCC cell lines with varying EMT phenotypes.

APTES silanization and Genipin crosslinking are well-established techniques for hydrogel functionalization [24–27], yet their combined use to stabilize long-term 3D tumor–fibroblast co-culture for functional drug screening has not been previously reported. Here, we optimize dual APTES/Genipin stabilization specifically to resist fibroblast-driven hydrogel contraction while preserving cell viability and assay robustness. We functionally validate the platform using patient-derived CAFs for clinically relevant drug screening.

Microfluidics offers precise control over microenvironmental parameters, including oxygen and nutrient gradients, mechanical forces, and chemical cues, thereby closely mimicking in vivo tumor conditions [28, 29]. Additionally, microfluidic miniaturization reduces the number of primary cells needed for experiments and enables multiplexed, parallel assays for functional drug screening [30, 31]. Altogether, we demonstrated that our platform supports long-term, physiologically relevant 3D tumor–fibroblast co-cultures, enabling robust quantitative readouts for tumor invasion, matrix remodeling, and drug response via live-cell imaging, combined with a semi-automated analysis workflow. Our work bridges breakthrough materials engineering with microfluidic precision, establishing a versatile proof-of-concept tool for clinical translation, mechanistic studies of tumor-fibroblast interactions, and high-content functional drug screening.

2 | Experimental Section

2.1 | Microfluidic Device Fabrication

Microfluidic devices were designed in AutoCAD 2024 (Autodesk, San Rafael, CA, USA), and a chromium photomask was prepared via Heidelberg μPG 101 direct writing. SU-8 features (200 ± 5 μm height) were patterned on silicon wafers using Karl Suss MABA6 photolithography. Molds were silanized with perfluorooctyl trichlorosilane (Sigma PFOCTS) to create an anti-adhesion layer. PDMS (Sylgard 184) was mixed (10:1), degassed, cast (30 g), cured at 70°C for 4 h, and plasma-bonded to cleaned glass slides. Inlets (1 mm) and outlets (3 mm) were punched; devices were annealed at 90°C for ≥48 h to reestablish hydrophobicity and prevent gel leakage. The full design layout of the microfluidic chip is provided as File S1 to support reproducibility and adaptation.

2.2 | Cell Culture Maintenance

2.2.1 | Cell Lines

HNSCC cell lines UT-SCC-19A (laryngeal carcinoma) and UT-SCC-44 (gingival carcinoma) were provided by Turku Uni-

versity Central Hospital, Finland. These lines were originally derived from recurrent and metastatic HNSCC, respectively, and were selected based on their differential sensitivity to Cisplatin, as previously described in Lepikhova et al. [7].

Normal human foreskin fibroblasts BJ (ATCC CRL-2522), hTERT-immortalized cancer-associated fibroblasts (PF179T), and LNCaP prostate cancer cells were obtained from the biobank of the Institute of Biomedicine, Cancer Research Unit, and FICAN West Cancer Centre Laboratory, University of Turku, and Turku University Hospital.

Cell lines UT-SCC-19A, UT-SCC-44, BJ, and patient-derived primary CAFs were cultured at standard growth conditions (incubator with 37°C, 5% CO_2) in DMEM/F-12 (Sigma, D8437), supplemented with 10% Fetal Bovine Serum (FBS, ThermoFisher, Gibco, 16140071), penicillin (100 units/mL), streptomycin (100 µg/mL), and antibiotics (Sigma, A5955). LNCaP cells were propagated in RPMI-1640 (Sigma–Aldrich, R8758).

2.2.2 | Patient-Derived Cells

Primary CAFs were isolated from surgical specimens of head and neck squamous cell carcinoma patients following permission and guidelines of the Institutional Review and Ethical Board of the Medical University of Lublin. Patient-derived postoperative tissue samples used in this study were obtained under Bioethics Committee approval of the Medical University of Lublin (KB-0024/134/09/2024; amendment to KE-0254/96/2020), with written informed consent for study participation and genetic testing obtained from the respective patients. Tumor tissue was mechanically dissociated and enzymatically digested as described in [32]. CAFs were plated in DMEM + 10% FBS and passaged after reaching 80% confluence. CAF identity was confirmed by qPCR (data not shown). Cells were used at passages 5–9. In this research, CAFs from a 63-year-old woman (location: 417770/01, right cheek tumor; highly mature (G-1) Squamous cell carcinoma; ICD-O code 8070/3; diagnosis: TNM: pT2, N2b, R0) were used for clinical translatability and patient validation.

2.3 | Cell Line Phenotyping

Cell line EMT phenotypes were characterized by immunofluorescence. Briefly, cells were seeded in 2D and cultured for 10 days before being fixed in 4% PFA, permeabilized with 0.1% Triton X-100, and immune stained with antibodies against Vimentin (ab16700, Abcam/1:200), pan-cytokeratin (ab7753, Abcam/1:100), EpCAM (21050-1-AP, Proteintech/1:100), N-cadherin (sc-393933, Santa Cruz/1:10), TWIST1 (ab50581, Abcam/1:100), ZO1 (#33-9100, Thermo Fisher Scientific/1:100), αSMA (ab5694, Abcam/1:100), Fibronectin (ab6328, Abcam/1:100), S100A4 (ab19789, Abcam/1:100), and E-cadherin (#14472, Cell Signaling Technology/1:100). Then, their total fluorescence was quantified according to Supporting Information Section S1.2 IF Staining Quantifications.

2.4 | Optimization of Hydrogels for 3D Co-Culture

ECM composition was optimized in Ibidi 96-well angiogenesis plates using the "sandwich" method described by Afshan et al. [33]. For direct benchmarking, 5 µL hydrogel domes were prepared in parallel in a standard 96-well plate as an additional comparative 3D format. The ECM components were diluted to final concentrations: Matrigel (Corning, 356231; 2 mg/mL), COL I (Corning, 354236; 0.75 mg/mL), and HA (ThermoFisher Scientific, J66993-ME; 5% v/v; 10 mg/mL stock). HA stock was prepared by dissolving 100 mg HA sodium salt in 10 mL PBS with ions and gently stirring overnight at +4°C.

2.5 | Seeding and Hydrogel Polymerization in Microchips

A hydrogel-cell suspension (2.5×10^6 cells/mL; 1:1 cancer: fibroblast ratio) was sequentially injected into opposing gel ports to fill the central chamber. To prevent gel desiccation during polymerization, hydrogel domes were formed over the injection ports, and chips were placed in a sealed, humidified chamber for 30 min at 37°C. Following polymerization, DMEM/F-12 medium was added to the reservoirs, and the microfluidic devices were maintained at 37°C with 5% CO_2. All experiments were operated under static culture conditions (manual media exchange) rather than continuous perfusion. Culture medium was refreshed every 48 h (during drug treatment, media changes were performed every 24 h). Genipin (Sigma G4796) was used to crosslink and stabilize COL-based hydrogels due to its low cytotoxicity, offering a biocompatible alternative to conventional crosslinkers such as glutaraldehyde [34]. For the experiments reported here, Genipin was added to the gel precursor (Matrigel/COL/HA) at a final concentration of 500 µM immediately prior to gelation, and cells were embedded during polymerization within the microfluidic chambers.

2.6 | Surface Treatment for Hydrogel Adhesion

Plasma-activated PDMS and glass surfaces were treated with oxygen plasma (CUTE, Femto Science Inc.) at 20 W for 60 s (O_2 flow 8 sccm; chamber pressure 150 mTorr) and then silanized with 2% (v/v) (3-Aminopropyl) triethoxysilane (Sigma A3648) in MilliQ water for 2 h. Substrates were rinsed twice in ethanol, and dried under compressed N_2 gas to improve gel retention and to reduce fibroblast-induced gel contraction.

2.7 | Hydrogel Contraction Assay

Brightfield images of gels in chips were obtained via Leica DMi1 (Leica GmbH, Microsystems) and EVOS M5000 (Thermo Fisher Scientific). Gel boundaries were manually traced in Fiji (ImageJ), and contraction was calculated as: Contraction (%) = $100 \times (1 - A_t/A_0)$, where A_0 and A_t are the initial and time-point areas, respectively. Data were analyzed in GraphPad Prism 9.5.1.

2.8 | Live/Dead Viability Assay

Microchips were stained with Hoechst 33342 (Sigma, 382069; 5 μg/mL) and Propidium Iodide (PI, Sigma, 537059; 1 μg/mL) for 30 min at 37°C. 3D fluorescent images were captured by Leica Thunder DMI8 (Leica Microsystems, Wetzlar, Germany) and Nikon ECLIPSE Ti confocal microscopes (Nikon Instruments Inc, Melville, NY). Instant computational clearing was applied via Leica LASX. Viability was calculated using AIVIA 14.1.0 (Leica, Microsystems; Supporting Information Section S1.1) as: $1 - \frac{\text{Propidium iodide}_{\text{counts}}}{\text{Hoechst33342}_{\text{counts}}}) \times 100$ [35], where dead objects are defined as nuclei with colocalized PI per the colocalization rule (see Supporting Information Section S1.1 Methodology, Tables S1 and S2, and Figure S1). The data were plotted using GraphPad Prism 9.5.1.

2.9 | Fourier Transform Infrared (FTIR) Spectroscopy

Fourier Transform Infrared (FTIR) spectroscopy with attenuated total reflection (ATR) spectra (Nicolet 6700) was recorded using a DTGS detector over 4000–400 cm^{-1} at 4 cm^{-1} resolution (10 scans/sample), with N_2 purging at room temperature. Hydrogel samples were dried on a 12-well plate, then placed on an ATR diamond under N_2 flow. The analysis was performed using OMNIC (Thermo Fisher Scientific, USA) and Grams AI software (Thermo Fisher Scientific, USA).

2.10 | Rheometry

Rheological measurements were performed using a strain-controlled rheometer (MCR-502, Anton Paar) equipped with a cone-and-plate geometry (diameter: 50 mm; cone angle: 2°). Samples were prepared as described in Section 2.4 and stored at 4°C for 12 min before being loaded into the measuring geometry, which was initially maintained at 4°C. All samples undergo the same thermal history: a constant temperature of 4°C for 200 s, followed by a ramp at 0.1°/s to 37°C, after which it is maintained constant. The evolution of the viscoelastic properties over time is followed using Small Amplitude Oscillatory Shear (SAOS) rheology, which involves applying a small-amplitude strain oscillation (γ_0 = 1%) at a constant frequency (1 Hz) and recording the storage and loss moduli. Viscoelastic spectra are measured using frequency-sweep tests, in which the angular frequency varies from 0.1 to 100 rad/s. The onset of large deformations is studied using amplitude-sweep tests, in which the strain amplitude varies from 10^{-5} to 10 at a frequency of 1 Hz.

2.11 | Drug Treatments

Cisplatin (Tocris) dissolved in 0.89% NaCl was administered at a physiological range of 1–10 μM after 6 days of 3D culture. Treatment lasted for 96 h, with daily drug renewal. Live/dead assay was used to determine viability; IC_{50} values were obtained via four-parameter Hill fitting in Python 3.11.11 (Google Colab) using log-transformed concentrations. These fits were exploratory and intended to provide approximate, comparative IC_{50} estimates rather than definitive pharmacological parameters.

2.12 | Immunofluorescence (IF) Stainings of Hydrogels

Samples were fixed in 2% PFA, permeabilized with 0.5% Triton X-100, and blocked in 3% BSA. Primary antibodies, anti-Vimentin (ab16700, Abcam/1:200), anti-pan-cytokeratin (ab7753, Abcam/1:100), anti-ZO1 (33-9100, Thermo Fisher Scientific/1:100), and Ki67 (ab15580, Abcam/1:100), were incubated overnight at 4°C, followed by PBS washing. Secondary antibodies (goat anti-mouse IgG-Alexa Fluor Plus 555 #A32727/1:200 and anti-rabbit IgG-Alexa Fluor Plus 488 #A32731/1:200; Thermo Fisher Scientific, USA) were incubated overnight at 4°C. Afterward, the samples were counterstained for actin filaments using Phalloidin Alexa Fluor 647 (#8940S, Cell Signaling Technology/1:50) and DNA/nucleus with Hoechst 33342(405 nm/1:1000, Sigma, 382069). Imaging was performed on a Nikon ECLIPSE Ti and a Zeiss LSM980 (Airy2/Elyra7). Z-stacks captured via EC Plan-Neofluar 10×/0.3 objective across five detection channels and processed in ZEN Blue with LSM Plus and extended-depth-of-focus methods.

2.13 | Statistical Analysis and Data Visualization

All quantitative data were analyzed and visualized using GraphPad Prism 9 (Prism v9.5.1) unless otherwise stated. IC_{50} values were calculated from chip-level normalized data, with a minimum of two independently seeded chips per condition (each on a separate slide, $n \geq 2$), using nonlinear regression with a four-parameter Hill equation (4PL) and 95% confidence intervals in Python (Python 3.11.11, Google Colaboratory).

For hydrogel contraction or area retention measurements, values were normalized to the total chip surface area to account for differences between chips, yielding relative retention (%) per chip. For drug-response/viability assays, raw measurements were normalized per chip to the corresponding vehicle control (control = 100% viability), unless otherwise indicated. Background correction or blank subtraction was applied where appropriate. No data transformations were applied unless explicitly stated.

Experiments were performed in two independent runs, each conducted on a different day. For each condition, a minimum of two chips were independently seeded on separate slides, with up to four conditions per slide. Each chip was considered an independent experimental unit for statistical analysis. Multiple non-overlapping fields of view were acquired per chip and averaged to generate a single chip-level value. Chip-level values were then used for all statistical comparisons ($n \geq 2$ chips per condition; more when additional slides were seeded).

Data are presented as mean ± standard deviation (SD) unless otherwise stated. Parametric data were analyzed using two-way ANOVA (two-sided), followed by Dunnett's post-hoc test for comparisons versus control or Sidak's post-hoc test for pairwise comparisons, as specified in figure legends. Non-parametric distributions were analyzed using Kruskal–Wallis tests with Dunn's multiple comparisons post hoc test. Comparisons between two independent groups were performed using two-sided unpaired t-tests or two-sided Welch's *t*-tests where variance was unequal. Comparisons of a single group against a fixed reference value

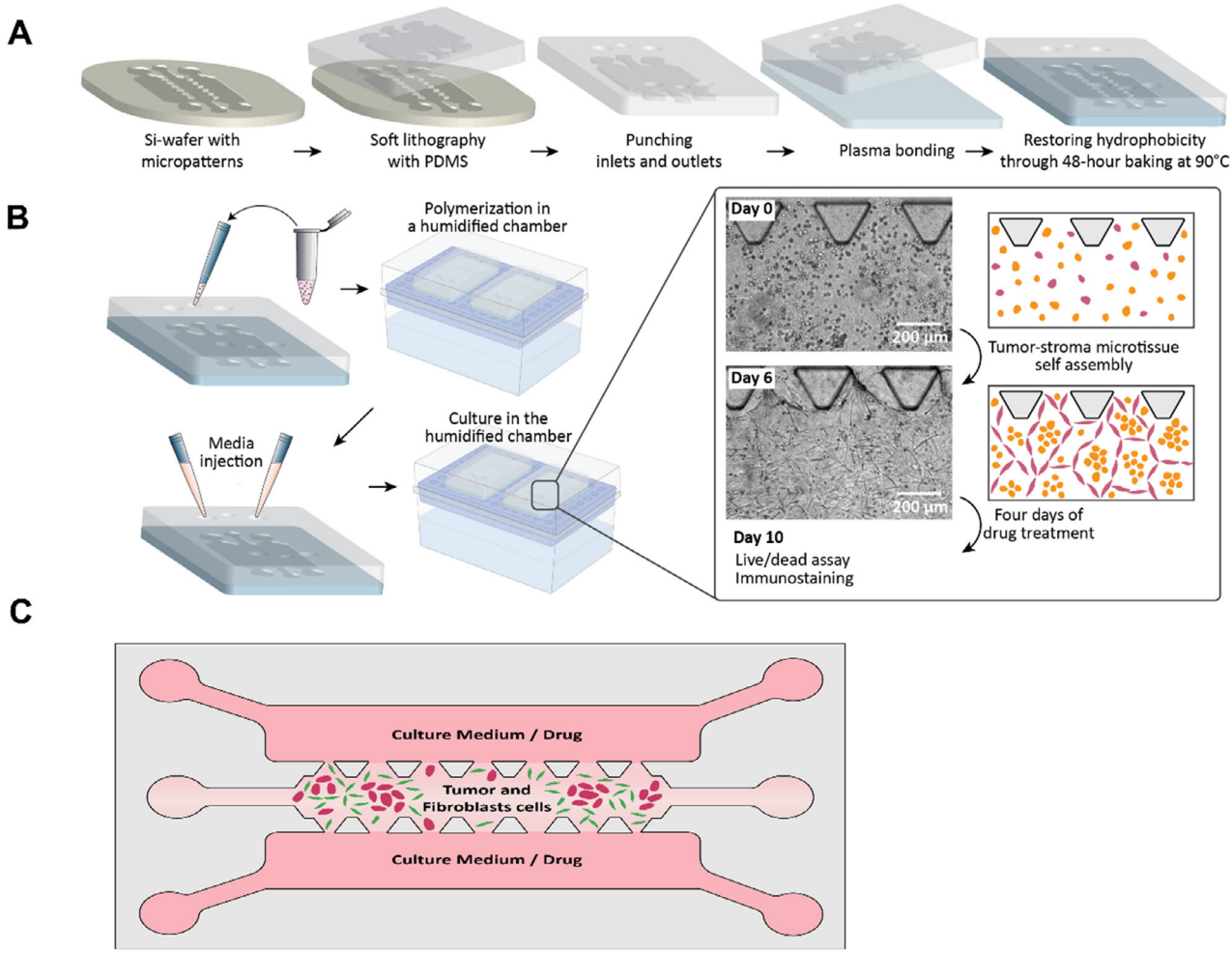

FIGURE 1 | Overview of microfluidic platform development. (A) Schematic of microfluidic chip fabrication. PDMS devices were generated by soft lithography using SU-8 patterned silicon wafers, punched to create inlet/outlet ports, and irreversibly bonded to glass coverslips via oxygen plasma activation (created with Adobe Illustrator 29.0). (B) Hydrogel loading and cell encapsulation workflow. Tumor cells and fibroblasts were co-seeded in a Matrigel/COL/HA (Mat/COL/HA) matrix crosslinked with Genipin and injected into the central chamber. Devices were cultured for 6 days to allow microtissue formation, followed by 4 days (96 h) of drug treatment. (C) Schematic representation of the microfluidic chip layout showing the spatial distribution of tumor cells and fibroblasts within the central hydrogel chamber and adjacent side channels used for media perfusion and drug delivery.

were performed using two-sided one-sample *t*-tests. All tests were two-sided with a significance level of $\alpha = 0.05$. Post-hoc analyses were performed with family-wise $\alpha = 0.05$ as implemented in Prism. Significance levels are indicated as: $^{*}p < 0.05$, $^{**}p < 0.01$, $^{***}p < 0.001$, $^{****}p < 0.0001$. No outliers were excluded.

3 | Results

3.1 | Microfluidic Device Engineering and Hydrogel Stabilization Strategy for Generating Complex Tumor–Stroma Microtissues

3.1.1 | Design and Stabilization of Composite Hydrogels for 3D Tumor–Stroma Culture

To recapitulate the structural and functional features of tumor–stroma interactions within a 3D microfluidic environment (Figure 1A), we designed a composite hydrogel system stabilized with Genipin crosslinking and covalently anchored to the chip surface by APTES. Fibroblasts, particularly CAFs, are highly contractile and remodel the surrounding ECM through force generation and biochemical signaling. Cancer cells, especially aggressive ones, can further enhance ECM degradation and remodeling, often resulting in matrix compaction and architectural collapse over time. A robust hydrogel is thus critical for maintaining long-term culture stability and preserving the tumor niche microarchitecture (Figure 1B,C).

We incorporated Genipin, a naturally derived crosslinker, into a composite Matrigel/COL/HA (Mat/COL/HA) hydrogel to reinforce its internal network via covalent interactions with primary amines, while simultaneously preserving the functional groups required for subsequent anchoring to the chip through APTES functionalization. Our composite hydrogel contains COL I (0.75 mg/mL), HA (5% v/v), and Matrigel (2 mg/mL), providing the essential structural and basement-membrane components for tumor–fibroblast co-culture; this formulation was selected following preliminary optimization experiments [32, 33, 36, 37]. Initial screening in 96-well plates using LNCaP/fibroblast co-

cultures identified a concentration of 500 μM Genipin as optimal for minimizing hydrogel contraction, while remaining nontoxic to tumor cells or fibroblasts, thereby fully supporting cell viability and the formation of tumor-like morphologies (data not shown).

3.1.2 | FTIR Investigation of Genipin-Mediated Crosslinking

To validate matrix crosslinking and evaluate chemical functionality retention, FTIR–ATR spectroscopy was performed on Genipin alone, native Mat/COL/HA hydrogel, and Genipin-crosslinked hydrogels after 2 h incubation at 37°C (Figure 2A,B). A distinct increase in the 1300–1450 cm^{-1} region (Figure 2A) corresponds to CH_2 bending and wagging vibrations, consistent with protein backbone reorganization following crosslinking [38]. The peak at 1037 cm^{-1}, linked to —OH reorganization and potential ether or ester bond formation, also shifted slightly. Notably, a detectable signal at 1106 cm^{-1}, corresponding to free Genipin, confirms that a portion remains unreacted—crucial for preserving reactive sites for chip functionalization [38].

Analysis of the Amide I (1700–1600 cm^{-1}) and Amide II (1500–1600 cm^{-1}) bands in FTIR-ATR revealed shifts indicative of Genipin–protein interactions (Figure 2A). The Amide II band, in particular, moved from ~1550 to ~1570 cm^{-1}, possibly reflecting NH_3^+ symmetric bending interactions [39, 40]. A concurrent rise in absorbance at ~1400 cm^{-1} suggests the formation of tertiary amine linkages and further crosslinking [38].

In the crosslinked formulation (Figure 2B), a reduction in the CH_2 symmetric stretching band at 2833 cm^{-1} was observed, consistent with increased molecular packing and network ordering upon Genipin crosslinking [41]. A modest reduction in the broad band at 3284 cm^{-1}, associated with O—H and N—H stretching, suggests partial consumption of hydroxyl and amine groups via hydrogen bonding or covalent interaction with Genipin [39, 40].

3.1.3 | Gelation and Viscoelastic Properties of Hydrogels

Time-resolved rheometry (Figure 2C) at fixed angular frequency (ω = 6.26 rad/s) shows that both formulations start as viscous liquids ($G'' \approx 0.1$ Pa, $G' \ll G''$) and undergo gelation when the storage modulus G′ surpasses the loss modulus G″ at the gel time t_g. The native formulation (without Genipin) gels more rapidly ($t_g \approx 60$ s), and G′ rises sharply before slowly approaching a plateau of ≈8 Pa for $t > 8000$ s. The Genipin-containing formulation shows delayed gelation ($t_g \approx 100$ s) and slower initial stiffening, but G′ increases steadily over extended times. Eventually, it overtakes the native sample at ≈1 000 s and continues to grow without plateauing even after 30 h (data not shown); at t ≈ 12 000 s and G′ ≈ 12 Pa. These contrasting kinetics support the presence of an additional, slower covalent crosslinking process in the Genipin formulation, likely involving progressive reaction of amine groups.

Frequency sweeps (Figure 2D) performed at $t \approx 12\,000$ s over three decades of angular frequency confirm that both systems are solid-like: G′ exceeds G″ across the entire ω range sampled. Consistent with the time-sweep results, gels formed with Genipin are systematically stiffer than native gels at this long time point, indicating that the additional crosslinks accumulated over time increase network elasticity across experimentally relevant timescales.

We performed strain-amplitude sweeps using large-amplitude oscillatory shear to assess gel failure (Figure 2E). At small strain amplitudes, the stress is linear with strain, indicating an intact elastic network. Nonlinearity appears above $\gamma \approx 0.1$, and the stress reaches a peak corresponding to network failure. The failure signatures differ: Genipin-containing gels exhibit a higher stress-at-break followed by an abrupt stress collapse (brittle-like failure), whereas native gels show a lower failure stress and a more gradual stress decay consistent with ductile-like fracture.

Together, the FTIR data and rheology indicate that Genipin induces covalent bond formation while leaving a measurable population of —OH/—NH_2 groups. Despite clear spectroscopic evidence of crosslinking, the bulk storage modulus increases only modestly after 3 h (G′ ≈ 8–12 Pa), suggesting that internal stiffening alone is insufficient to fully prevent cell-driven compaction. Instead, long-term maintenance of microarchitecture likely reflects a combined effect: progressive reinforcement of Genipin-mediated networks, combined with covalent anchoring to the chip surface via plasma/APTES (Figure 2F). This dual functionalization therefore reconciles modest changes in bulk modulus with the pronounced macroscopic stability observed during extended tumor–stroma culture.

3.2 | APTES Functionalization and Genipin Crosslinking Synergistically Enhance Hydrogel Stability and Limit Matrix Contraction in 3D Tumor–Stroma Microtissues

We established 3D tumor–fibroblast co-cultures using two HNSCC cell lines with distinct epithelial–mesenchymal phenotypes. UT-SCC-19A maintains strong epithelial character (pan-cytokeratin^{+++}/vimentin^{-}/E-cadherin^{++}; Supplementary Figure S2, Table S3), while UT-SCC-44 exhibits partial EMT with co-expression of epithelial and mesenchymal markers (pan-cytokeratin^{++}/vimentin^{+++}/E-cadherin^{+}/N-cadherin^{+}; Figure S2, Table S3). This phenotypic diversity enables modeling of both well-differentiated and aggressive tumor behaviors. BJ fibroblasts, a well-characterized human dermal fibroblast line, served as a model stromal component for technical platform development, providing reproducible contractile and matrix-remodeling activity. Throughout Sections 3.2–3.4, we refer to these experiments as "tumor-fibroblast co-cultures." Validation with patient-derived cancer-associated fibroblasts (CAFs), representing authentic tumor-fibroblast interactions, is presented in Section 3.5. It should be noted that the experiments presented in Sections 3.1–3.4 are primarily designed for platform development and mechanistic characterization of matrix stabilization, hydrogel contraction resistance, spatial organization, and drug response readouts. The patient-derived CAF experiments presented in Section 3.5 serve as proof-of-concept, demonstrating the platform's compatibility with clinically relevant primary stromal cells.

Following FTIR–ATR validation of Genipin-mediated crosslinking and the retention of reactive groups (Figures 2A,B), we next investigated the macroscopic impact of Genipin and APTES

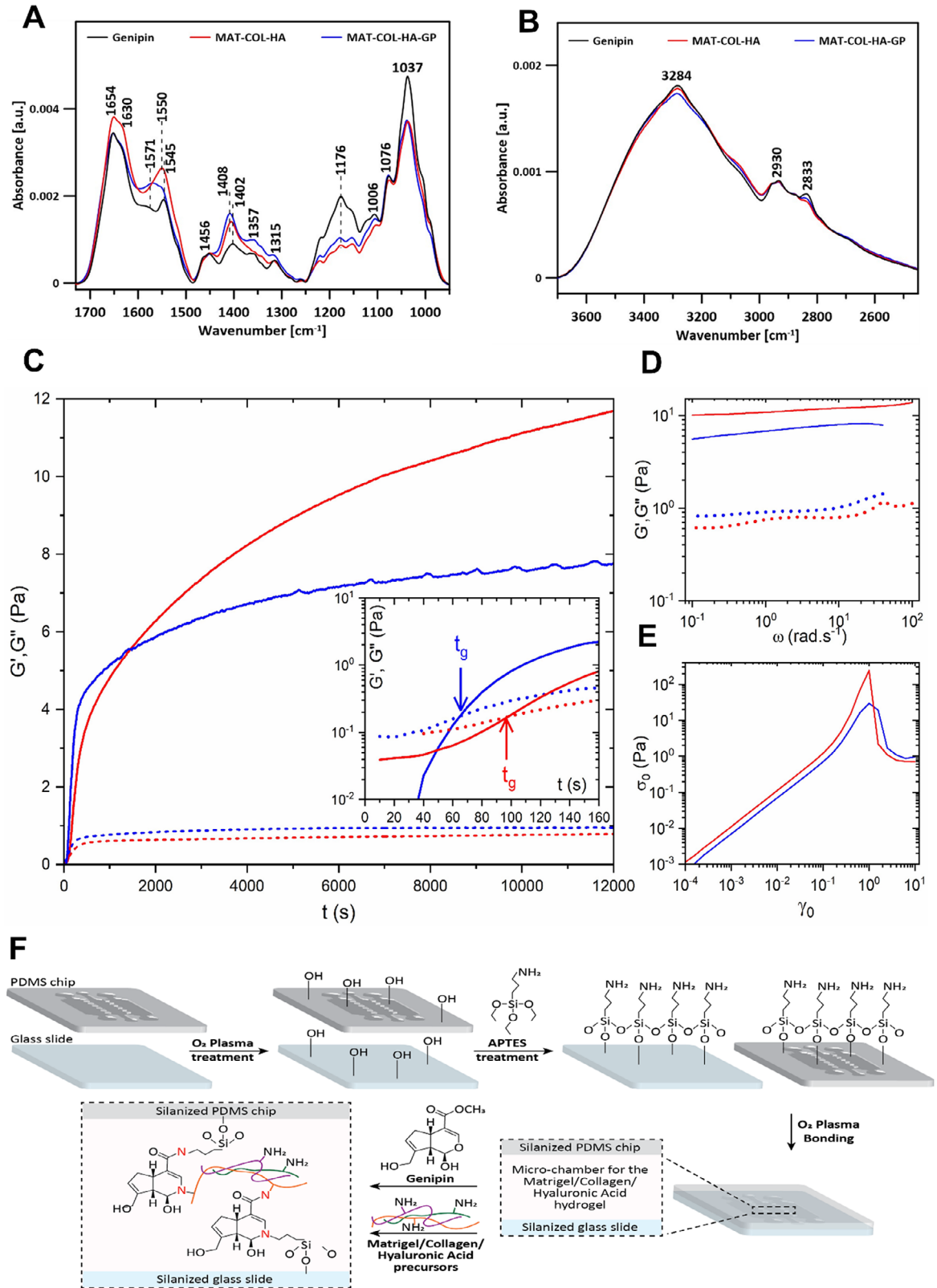

FIGURE 2 | FTIR, rheological characterization, and dual-surface functionalization strategy of Genipin-modified Mat/COL/HA hydrogels. (A) FTIR-ATR spectra (950–1730 cm^{-1}) comparing Mat/COL/HA hydrogels with and without Genipin. Key shifts in amide I/II and C–O/C–N stretching regions indicate successful crosslinking and structural rearrangement. (B) FTIR-ATR spectra (2450–3700 cm^{-1}) highlighting changes in CH_2, O—H, and N—H stretching bands. Decreases at 3284 and 2833 cm^{-1}, along with persistent signals, suggest partial retention of functional groups relevant for subsequent surface anchoring. (2C) Time-sweep ($\omega = 6.26$ rad/s). Native gels (blue curve) gel faster ($t_g \approx 60$ s) and plateau (~8 Pa); Genipin gels (red curve) gel later (t– ≈ 100 s) but continue stiffening, reaching ≈12 Pa at 12 000 s. (D) Frequency sweep ($t \approx 12\,000$ s). G′ exceeds G″ across three decades of ω for both samples, confirming solid-like behavior; Genipin-crosslinked gels are consistently stiffer. (E) Strain-amplitude sweep. Linear elastic response

surface functionalization on hydrogel contraction in 3D tumor-fibroblast models. Preserving the hydrogel architecture over time is critical to maintaining spatial, tissue-like organization and enabling long-term 3D co-culture in a structurally stable environment.

Matrix contraction was quantified by measuring hydrogel areas over time, supplemented with two HNSCC cell lines (UT-SCC-19A and UT-SCC-44), which have been characterized as representing squamous epithelial versus partial epithelial-to-mesenchymal transition (pEMT) phenotypes, respectively (see Figure S2). Four different experimental conditions were tested: (1) untreated control, (2) APTES surface functionalization only, (3) Genipin (500 μM) crosslinking only, and (4) APTES + Genipin combined (Figure 3A,B). On day 1, most conditions maintained the hydrogel area with minor contraction. However, UT-SCC-44 co-cultured with BJ fibroblasts showed rapid matrix collapse, with the hydrogel area reduced to ~13.8% by day 1, indicating pronounced contractile behavior even at early time points. This effect was markedly attenuated in Genipin-treated gels (Figure 3A).

By day 6, untreated cultures exhibited severe matrix contraction. UT-SCC-44 monocultures contracted almost completely and retained just ~1.5% of the original hydrogel area, while co-cultures with BJ fibroblasts retained ~7% of the original area, resulting in dense, spherical aggregates packed with cells (Figure 3A,C). In contrast, Genipin-crosslinked conditions showed significant stabilization, with 72% area preserved in UT-SCC-44 monocultures and 53% in UT-SCC-19A/BJ co-cultures. Notably, the combination of Genipin crosslinking and APTES surface functionalization led to near-complete hydrogel stabilization, even observed with the highly contractile UT-SCC-44/BJ model (95% retained area).

Interestingly, co-cultures of UT-SCC-19A/BJ cells in the APTES plus Genipin condition still exhibited modest contraction (Figure 3A,B), whereas UT-SCC-44/BJ co-cultures showed more complete stabilization. This difference reflects the distinct cellular organization patterns: UT-SCC-19A displays strong epithelial features (pan-cytokeratin +/vimentin−) character with E-cadherin-mediated cell–cell junctions, resulting in coordinated collective contractile forces concentrated at tumor–fibroblast boundaries. In contrast, UT-SCC-44's partial EMT phenotype produces more distributed, individual cell traction forces that are effectively constrained by the crosslinked matrix (Supplementary Figure S3). This very motile cell line does not form prominent cell–cell junctions with each other nor with fibroblasts.

Stabilized hydrogels strongly supported the emergence of biomimetic tissue-like architecture, reminiscent of the architecture observed in squamous carcinomas (Figure 3C, top and bottom panels). Immunofluorescence (IF) staining validated the spontaneous formation of structural patterns in stabilized/crosslinked 3D co-cultures. Without crosslinking, the hydrogel rapidly collapsed into dense, disordered, and featureless clusters. In contrast, Genipin-crosslinking promoted an organized distribution of epithelial and stromal cells within the matrix, with minimal deformation of the hydrogel boundary.

In 3D cultures of the less aggressive UT-SCC-19A cells (Figure 3C, top panel), Genipin cross-linking promoted the spontaneous formation of "epithelial-like cell clusters" within the Mat/COL//HA matrix, surrounded by fibroblast-rich stroma. The combination of Genipin and APTES improved matrix resilience, prevented cell escape from the matrix, and enabled localized ECM remodeling.

Remarkably, even the highly invasive UT-SCC-44/BJ co-cultures (Figure 3C, bottom panel) exhibited self-organized but spatially homogeneous tumor-fibroblast architecture, with tumor cells interspersed throughout a fibroblast-rich matrix, an architecture that this cell line typically fails to form under 2D conditions (Figure S3). This suggests that ECM crosslinking supports tissue-like spatial organization, and constrains tumor cell plasticity, likely through biophysical cues that recapitulate key features of the native tumor microenvironment. Together, these findings demonstrate that the combination of Genipin crosslinking and APTES-mediated chip functionalization is critical for hydrogel stabilization, initiation, and maintenance of 3D structure, promotes cellular organization reminiscent of squamous epithelial architecture, and supports spontaneous spatial organization in tumor-fibroblast microtissues. This integrated dual strategy enables long-term 3D co-culture and promotes the formation of complex tissue-like structures that go beyond simple organoid monocultures and instead reflect genuine pathophysiological features observed in most solid tumors. Using matrix crosslinking and stabilization, we established a robust platform for mechanistic in vitro studies, including therapeutic chemosensitivity testing in a physiologically relevant 3D environment.

3.3 | Combined APTES Functionalization and Genipin Crosslinking Preserve Hydrogel Integrity, Enhancing Viability and Spatial Organization in 3D Tumor–Stroma Co-Cultures

Building on our demonstration that Genipin crosslinking combined with APTES surface functionalization effectively stabilizes hydrogel architecture and limits contraction (Figure 4), we aimed to show that silane functionalization of both PDMS and glass substrates enhances cell viability and, in combination, more effectively prevents matrix contraction (Figure S4). We next evaluated how this matrix stabilization impacted long-term cell viability, proliferation, and 3D spatial organization in tumor-fibroblast co-cultures.

In native hydrogels (control and APTES-only), early matrix contraction led to scaffold collapse and dense cell clustering by Day 3, followed by increasing cell stress and death within aggregates by Day 6, and substantial cell escape to the chip

is preserved up to $\gamma \approx 0.1$; beyond this, the stress peaks at the onset of network failure. Genipin gels show a higher stress-at-break with abrupt collapse (brittle-like), while native gels fail more progressively (ductile-like). (F) Schematic representation of the dual-surface functionalization strategy. Plasma-activated PDMS and glass were silanized using APTES to enable covalent bonding to Genipin-crosslinked hydrogels via residual hydroxyl and amine groups.

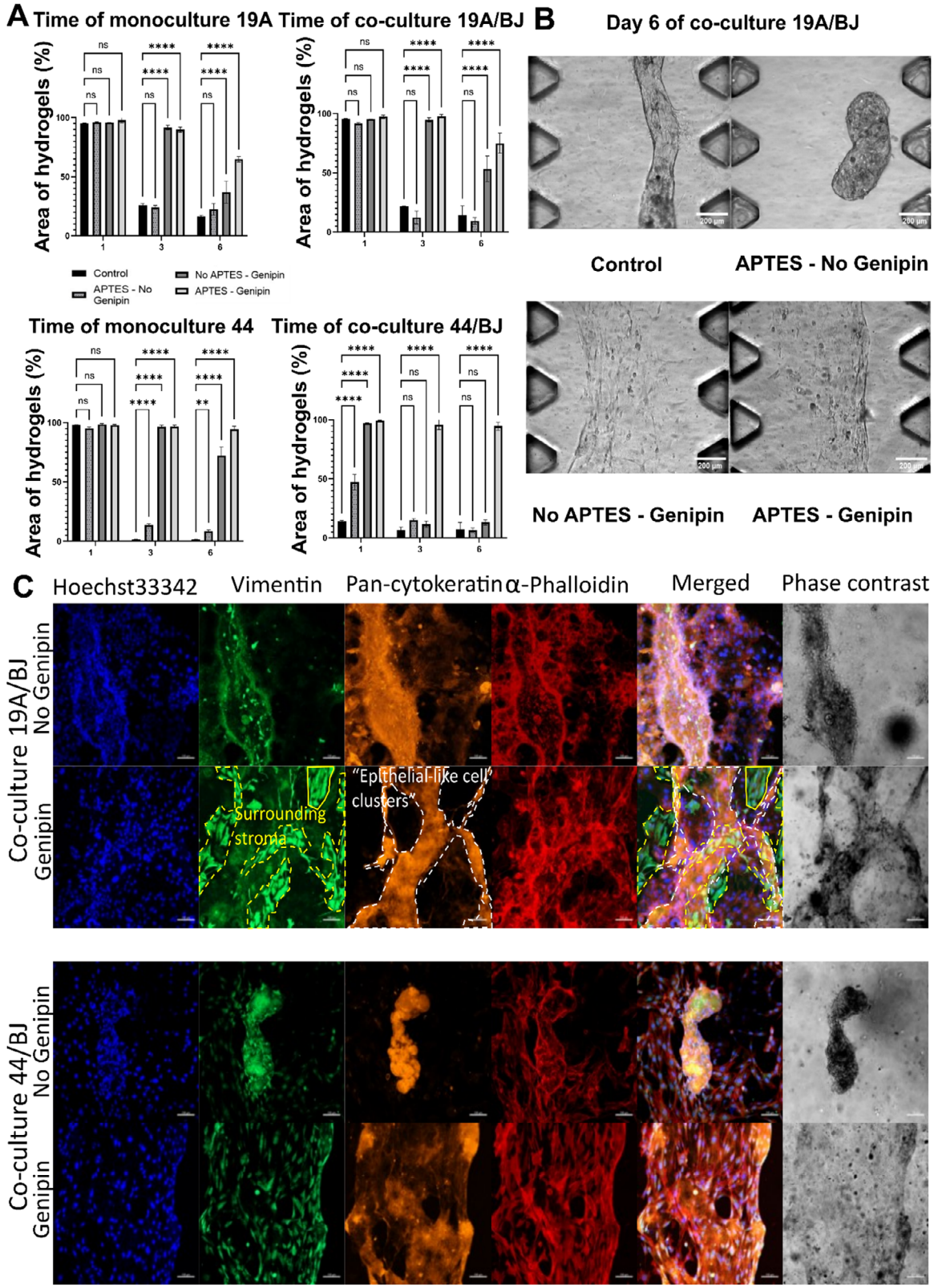

FIGURE 3 | Synergistic effect of APTES functionalization and Genipin crosslinking on hydrogel stabilization in 3D tumor–fibroblast models. (A) Quantification of hydrogel area retention over 6 days for UT-SCC-19A and UT-SCC-44 cell lines cultured in mono- or co-culture with BJ fibroblasts. Four conditions were assessed: untreated, APTES-only, Genipin-only (500 μM), and APTES + Genipin. The retention of hydrogel areas was calculated as the hydrogel area normalized to the total chip surface area. Data represent mean ± SD of $n = 3$ independently seeded chips per condition, each considered an independent experimental unit. Statistical analysis was performed in GraphPad Prism 9 (v9.5.1) using two-way ANOVA (two-sided) with Dunnett's post hoc test versus the untreated control. Normality was assessed using the Shapiro–Wilk test ($\alpha = 0.05$). Significance threshold was set at $\alpha = 0.05$. Exact p-values are reported in the figure. Significance: *$p < 0.05$; **$p < 0.01$; ***$p < 0.001$; ****$p < 0.0001$. (B) Brightfield images of UT-SCC-19A/BJ

surface by Day 10 (Figure 4A). Immunofluorescence revealed that both tumor (pan-cytokeratin$^+$/vimentin$^-$) and stromal (pan-cytokeratin$^-$/vimentin$^+$) cells escaped the matrix and formed disorganized 2D layers (Figure 4B, top panel). In contrast, crosslinked hydrogels preserved matrix architecture and promoted the formation of structured epithelial-like clusters surrounded by stromal fibroblasts, mimicking tissue-like organization (Figure 4B, bottom panel).

Cell viability was significantly higher in APTES–Genipin-stabilized hydrogels than in contracted conditions, where dense clusters showed increased cell death (Figure 4C). Viability analysis further distinguished matrix-resident from escaped cells, demonstrating that matrix retention strongly correlated with survival (Figure 4D). Ki-67 staining confirmed active proliferation in stabilized hydrogels, whereas contracted cultures showed diminished proliferative capacity (Figure 4E).

High-resolution confocal imaging (Figure 4F) revealed organized structures in stabilized matrices, characterized by coherent F-actin organization (α-phalloidin) and uniform nuclear distribution (Hoechst), consistent with tissue-like cell-cell organization in 3D culture. These tissue-like features were absent in non-stabilized conditions.

Phenotypic differences between UT-SCC-19A and UT-SCC-44 were also preserved. UT-SCC-19A maintained strong epithelial traits, whereas UT-SCC-44 exhibited mesenchymal morphology and partial EMT characteristics (Figure S2). Notably, even the aggressive UT-SCC-44 line exhibited a spontaneous, self-organized, yet spatially homogeneous tumor–fibroblast architecture within stabilized matrices, underscoring the role of matrix stabilization in imposing spatial organization.

While we cannot definitively distinguish matrix-imposed spatial organization from active differentiation programs, the observed F-actin localization and organized architecture suggest the stabilized microenvironment supports cellular behaviors more representative of in vivo squamous epithelia than standard 2D culture. Together, these results underscore the synergistic role of Genipin crosslinking and APTES anchoring in maintaining hydrogel integrity and supporting long-term viability and self-organization of 3D tumor–stroma cultures. This provides a stable and biologically relevant platform for advanced drug testing and phenotypic analysis.

3.4 | Matrix Stabilization Modulates Single-Cell Morphometrics and Spatial Behavior in 3D Tumor–Fibroblast Co-Cultures

To complement the previous findings on hydrogel stability, cell viability, multicellular tissue organization, and phenotype (Figure 4), we also performed a detailed quantitative morphometric analysis at the single-cell level. This approach allowed us to precisely measure how hydrogel stabilization may influence tumor and stromal cell morphology and the spatial positioning of cells within tissue-like structures over time. Specifically, we analyzed 3D-reconstructed tumor and stromal cells cultured in native versus Genipin-crosslinked hydrogels, focusing on cell volume, surface area-to-volume ratio (SA:V), and bounding box dimensions (see Supporting Information Section S.1.1.4 for definitions). Quantitative metrics (volume, SA:V and bounding dimensions) were derived from 3D meshes reconstructed in Aivia 14.1.0 from the original z-stacks (see Supporting Information Section S.1.1). Segmentation QC (IoU) is reported in Table S2, and Supporting Information S2 (mesh rotation) and Supporting Information S3 (Aivia screen capture showing mesh overlap and per-object volume readouts) visually demonstrate the volumetric reconstructions underlying the results (Figure S1). These quantitative metrics provide deeper insight into how the structural integrity of the matrix shape cell behavior and organization beyond qualitative observations.

3.4.1 | Matrix-Driven Changes in Cell Volume and SA:V Indicate Distinct Morphological States

Figure 5A,B shows that in native, hydrogels, early cell clustering and contraction lead to reduced individual cell volumes and lowered SA:V ratios by Day 3, indicative of compaction and limited nutrient diffusion. Figure 5A shows that adding Genipin (with or without APTES) stabilizes average cell sizes and volume, while these vary over a broad range in native gels (average during the culture of 13 289 $\pm$ 6 623 μm for control and 12 769 $\pm$ 6 137 μm for APTES only vs. 19 304 $\pm$ 3 513 μm for APTES—Genipin). Similarly, SA:V area increases over time in native gels (from 0.26 on day 3 to 0.40 on day 10 for control and 0.29 on day 3 to 0.41 on day 10 for APTES only), while it is gradually reduced and stabilized in Genipin-crosslinked gels (from 0.46 on day 3 to 0.30 for APTES—Genipin condition; Figure 5B).

This is partly explained by the observation that by days 6 and 10, many cells escape the contracting matrix and instead adhere to the chip surface, adopting flattened, but also enlarged, morphologies characteristic of 2D adherent cell culture environments. In contrast, cells within Genipin-crosslinked hydrogels display a stable, consistent, slow increase in volume (Figure 5A) while maintaining low SA:V ratios throughout the entire 3D culture period (Figure 5B). This suggests that matrix stabilization supports sustained volumetric growth and prevents excessive surface spreading, favoring physiological cell–cell and cell–matrix interactions within a structured 3D microenvironment.

3.4.2 | Bounding Box Metrics Reveal Stabilization-Dependent Constraints on Migration and Expansion

Bounding box metrics (scheme in Figure 5C) provide spatial insight into cell positioning and spreading within the hydrogel.

co-cultures in the central chamber at day 6, comparing Genipin-crosslinked and native hydrogels. Scale bar: 200 μm. (C) Immunofluorescence staining of UT-SCC-19A/BJ (top) and UT-SCC-44/BJ co-cultures (bottom) after 10 days, showing Vimentin (mesenchymal marker), pan-Cytokeratin (epithelial marker), F-actin (Phalloidin), and nuclei (Hoechst 33342) stainings. Z-stack projections acquired using Zeiss LSM980 with 10× objective. Scale bar: 100 μm.

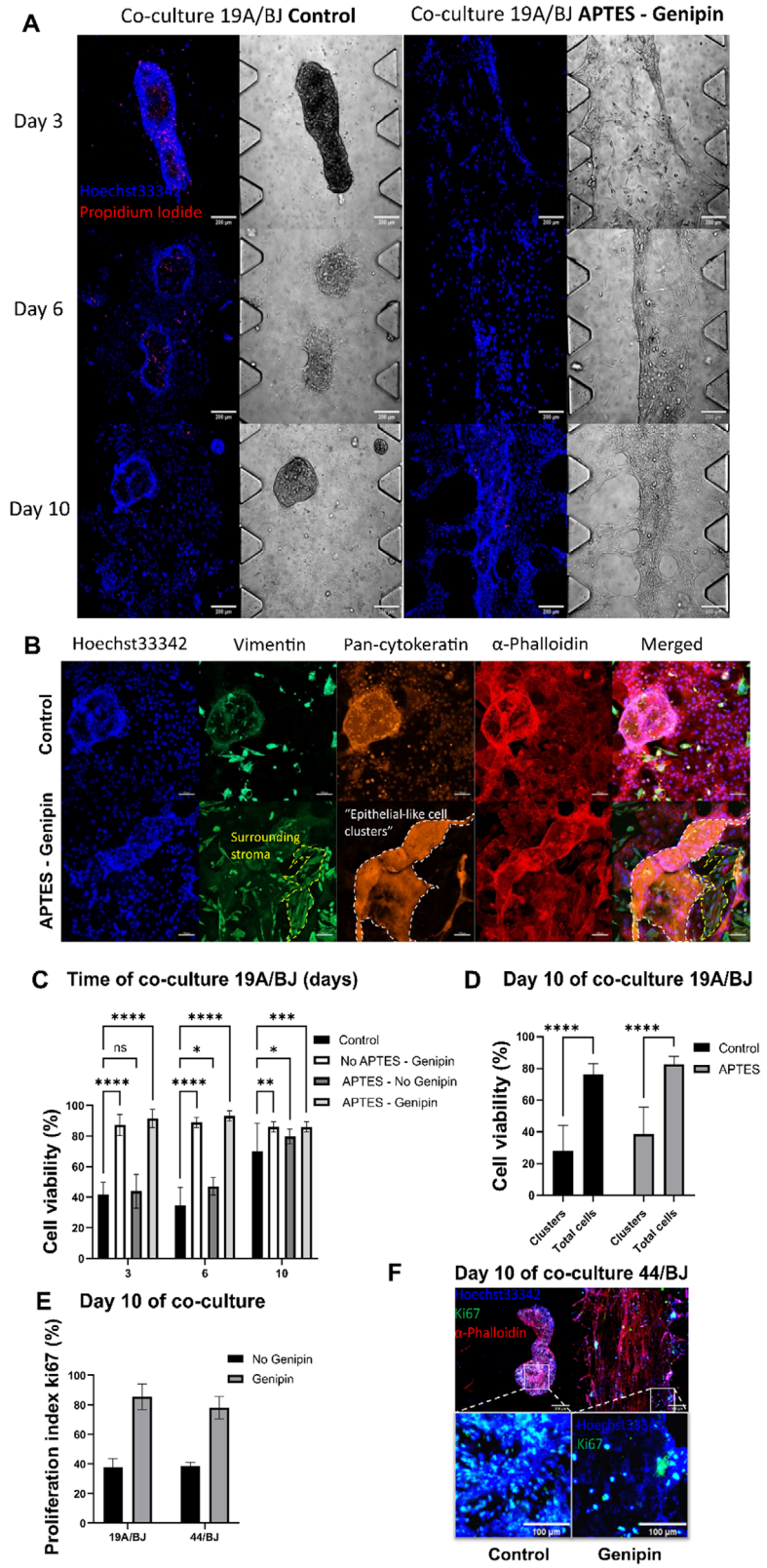

FIGURE 4 | Stabilization of hydrogel architecture via dual functionalization improves spatial organization and viability of tumor–fibroblast co-cultures. (A) Representative z-projection images of UT-SCC-19A/BJ co-cultures at days 3, 6, and 10 cultured in either native (non-Genipin-crosslinked, non-functionalized) or Genipin-crosslinked hydrogels anchored to APTES-functionalized chips. Images show phase contrast overlays with Hoechst 33342 (nuclei, blue) and Propidium Iodide (dead cells, red). Images acquired using Nikon ECLIPSE Ti confocal microscope; scale bar: 200 µm. (B) Immunofluorescence staining of UT-SCC-19A/BJ co-cultures at day 10 for control and APTES/Genipin conditions, showing Vimentin (mesenchymal), Pan-cytokeratin (epithelial), Phalloidin (F-actin), and Hoechst (nuclei). Images acquired using a 10× objective (Zeiss LSM980); scale bar: 100 µm. (C) Quantification of cell viability based on live/dead nuclear segmentation at days 3, 6, and 10 across experimental conditions. Viability was determined

In native hydrogels (control, or APTES only), the bounding depth decreases over time (from 71.1 μm on day 3 to 64.6 μm on day 10 for control; and 68.5 μm on day 3 to 60.0 μm on day 10 for APTES only), indicating vertical migration out of the matrix and onto the chip surface (Figure 5D). Concurrently, bounding width and height increase (control had a bounding width going from 20.6 μm on day 3 to 25.1 μm on day 10 and a bounding height from 21.4 μm on day 3 to 24.9 μm on day 10), reflecting lateral expansion typical of unanchored, disorganized 2D cultures (Figure 5E,F). Conversely, Genipin-crosslinked hydrogels exhibit increasing bounding depth (from 72.2 μm on day 3 to 85.7 μm on day 10 for APTES—Genipin condition) with stable lateral dimensions (±23 μm of bounding height and ±22 μm of bounding width for APTES—Genipin at different time points), consistent with deeper embedding and uniform expansion within the 3D matrix. These findings confirm that hydrogel crosslinking effectively prevents scaffold collapse and supports organized, tissue-like growth.

Together, these morphometric data extend the earlier viability and immunofluorescence results by quantitatively demonstrating how hydrogel crosslinking preserves physiological cell morphology and spatial organization. Stabilized hydrogels provide a permissive environment that supports sustained proliferation and epithelial-like organization, whereas native matrices lead to early compaction, cell stress, and disorganized migration despite rescued viability on 2D surfaces. These insights underscore the importance of the structural integrity of the matrix in shaping tumor–stroma co-culture behavior and highlight the value of crosslinked hydrogels for robust, biomimetic 3D tumor modeling and drug screening applications.

3.5 | Genipin-Crosslinked Hydrogel Microfluidic Models Enable Drug Sensitivity Profiling in Tumor–Stroma Co-Cultures

Having demonstrated that Genipin crosslinking preserves hydrogel integrity and supports long-term viability and organization of 3D microtissues, we next assessed the utility of our stabilized 3D model system for in vitro chemosensitivity testing. We focused on Cisplatin, a first-line agent in the chemotherapy of HNSCC for the past 30+ years, to examine how the structural integrity of the matrix and stromal interactions may affect therapeutic response in vitro.

3.5.1 | Clinical Relevance of the Cisplatin Dose Range

The range of cisplatin concentrations used (0–10 μM) reflected physiologically and clinically relevant exposures. Continuous infusion (40 mg/m^2/day) yields patient plasma levels ~10.7 μM (unbound ~0.57 μM), while intraperitoneal delivery and patient variability can raise unbound levels to ~7 μM. Shorter high-dose infusions (100 mg/m^2 over 3 h) yield unbound peaks ~6.7 μM [42–44]. This range spans both sustained therapeutic levels and clinical peak exposures.

3.5.2 | Cisplatin Sensitivity Differs Between Native and Stabilized 3D Cultures

Dose–response assays with UT-SCC-19A and UT-SCC-44 in co-culture with CAFs showed reduced viability in native hydrogels starting at ≥5 μM Cisplatin, while Genipin crosslinking preserved cell viability across all the doses (Figure 6A). This suggests hydrogel stabilization confers some protection by maintaining structural cues, but may also reinforce tumor–stroma interactions, which are known to support tumor cell survival and increase drug tolerance compared to monoculture conditions. In native matrices, we further distinguished responses between adherent ("bottom") and embedded or "clustered" cells (Figure 6B): adherent cells at the bottom of our chips exhibited higher drug tolerance, which is consistent with enhanced survival signaling via integrin-mediated cell survival pathways (e.g., FAK, PI3K/AKT pathways) in 2D adherent cell cultures. In contrast, embedded cells likely faced increased stress, nutrient and oxygen limitations, and impaired polarity, reducing cell viability and increasing the overall susceptibility to cytotoxicity.

3.5.3 | Stabilized Matrices Recapitulate EMT-Linked Drug Resistance

In crosslinked and stabilized hydrogels, UT-SCC-19A (epithelial) remained more sensitive to cisplatin than UT-SCC-44 (partial

by live/dead nuclear segmentation and expressed as the percentage of live nuclei relative to total nuclei per chip. For each chip, one to several non-overlapping fields of view were acquired. Each chip was considered an independent experimental unit ($n = 4$ per condition); field-of-view measurements were used for visualization only and not treated as independent replicates. (D) Day 10 viability in native hydrogels, quantifying cells retained within the matrix ("clusters") versus the total population, including cells that migrated on the chip surface and cells that aggregated within the matrix. For each chip, one or several non-overlapping fields of view were acquired. Each chip was considered an independent experimental unit (n = 4 per condition); field-of-view measurements were used for visualization only and not treated as independent replicates. (E) Ki67 proliferation index at Day 10 in UT-SCC-19A/BJ and UT-SCC-44/BJ co-cultures under native and crosslinked conditions. Quantification performed using semi-automated image analysis workflows is detailed in Supporting Information Sections S.1.1–S.1.2. For each condition, three non-overlapping ROIs were analyzed from a single chip. ROI-level measurements are presented as mean ± SD for visualization only; no statistical comparisons were performed, as only one chip per condition was analyzed. (F) Z-projection IF staining of UT-SCC-44/BJ co-cultures at day 10 in native versus crosslinked hydrogels. The top row presents full fields of view stained for Hoechst (nuclei, blue), Ki67 (proliferation, green), and α-phalloidin (F-actin, red). Scale bar = 200 μm. The bottom row shows corresponding higher-magnification zooms displayed as Hoechst+Ki67 overlays to emphasize nuclear morphology and proliferative status within selected regions. Scale bar = 100 μm. Statistical analysis was conducted on chip-level values in GraphPad Prism 9 (v9.5.1) using two-way ANOVA with Dunnett's post-hoc test, two-sided, $\alpha = 0.05$ (C) and Sidak's post-hoc test, two-sided, $\alpha = 0.05$ (D). Data are presented as mean ± SD. Significance: $^*p < 0.05$, $^{**}p < 0.01$, $^{***}p < 0.001$, $^{****}p < 0.0001$.

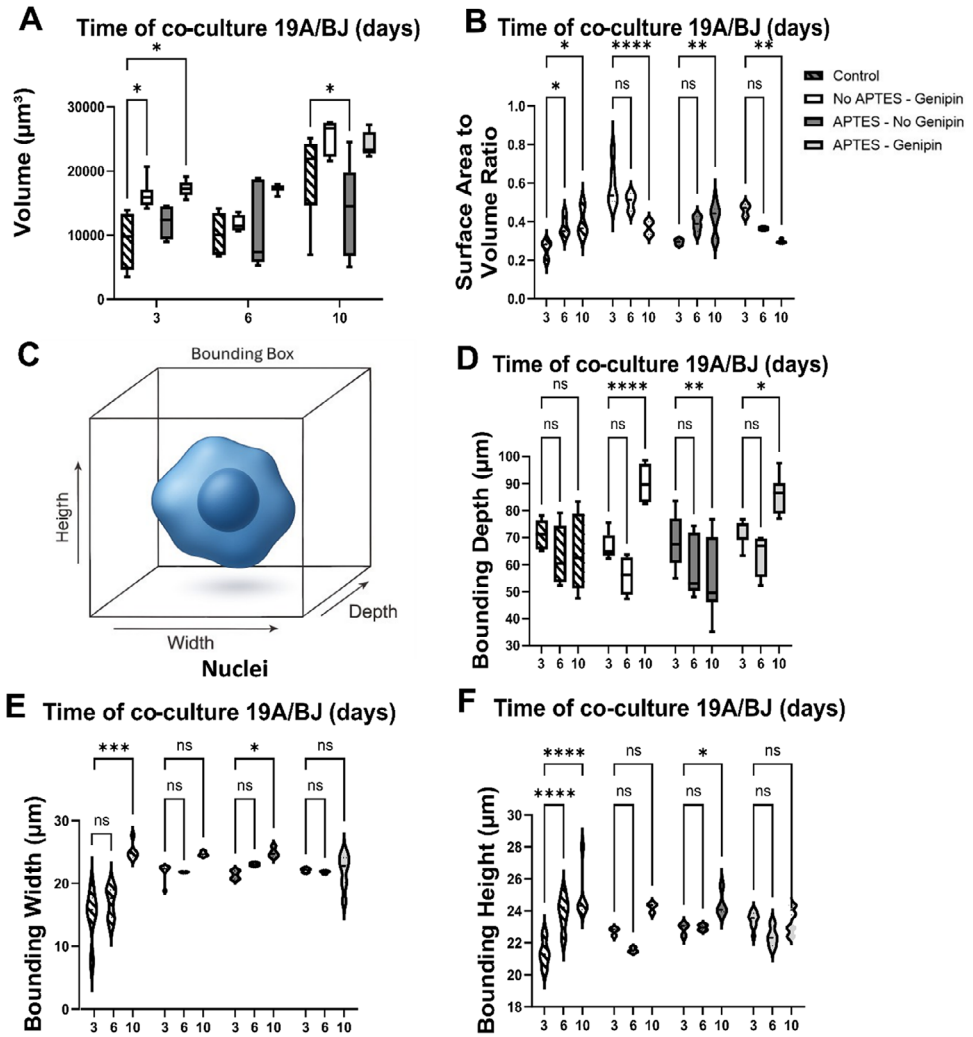

FIGURE 5 | Impact of APTES functionalization and Genipin crosslinking on single-cell morphology in 3D tumor–fibroblast co-cultures over time. Quantitative morphometric analysis of tumor and fibroblast nuclei cells at days 3, 6, and 10. (A) Cell volume (µm^3), (B) surface area-to-volume (SA:V) ratio, (C) bounding box dimensions, and orthogonal measurements—(D) bounding depth (µm), (E) bounding width (µm), and (F) bounding height (µm)—were extracted from 3D reconstructions using Aivia software. Volume and bounding depth are shown as box plots; SA:V, bounding height, and width as violin plots. The bounding box (C) illustrates X (width), Y (height), and Z (depth) dimensions used for spatial quantification. Image analysis workflow is detailed in Supporting Information Section S.1.1 (see also S.1.1.4 and Figure S1); Movies S2 and S3 illustrate representative mesh reconstructions and segmentation overlap. For imaging, one to several non-overlapping fields of view (FOVs) were acquired per chip; ROI-level measurements were summarized (averaged) to produce a single chip-level value used for downstream analysis. Per-chip quantification included ~1 000–4 000 nuclei depending on local cell density; data for each condition were pooled across $n = 4$ independently seeded chips (two chips per experimental run across two independent runs), totaling >4 000 nuclei per condition (minimum $n = 4$ chips per condition). Statistical comparisons were performed on per-chip summary values (biological replicates) in GraphPad Prism 9 (v9.5.1). Normality was assessed where applicable (Shapiro–Wilk test, $\alpha = 0.05$). Parametric comparisons used two-way ANOVA (two-sided) with Dunnett's post hoc test vs. control; all tests were two-sided, and significance was assessed at $\alpha = 0.05$ (post-hoc family-wise $\alpha = 0.05$). Data are presented as mean ± SD. Significance: *$p < 0.05$, **$p < 0.01$, ***$p < 0.001$, ****$p < 0.0001$.

EMT), confirming that the model at least partially captures intrinsic EMT-associated chemoresistance (Figure 6C). This stratification supports its application for phenotype-specific drug screening. Notably, in previous settings, fibroblasts and CAFs have consistently shown resistance to chemotherapeutic drugs within the tested concentration range, with minimal impact on their viability at doses that effectively inhibit tumor cell growth or induce cell death [15, 33]. This further validates the relevance of the co-culture system for differential drug response assessment.

3.5.4 | Fibroblast Co-Culture Confers Stromal-Mediated Chemoprotection

Fibroblast co-culture significantly increased resistance to Cisplatin in both models (Figure 6D,E) compared to tumor cell monoculture. Comparative viability analysis at the clinically relevant fixed concentrations of 5 and 10 µM (Figure 6C–E) directly demonstrates this stromal chemoprotective effect. Exploratory curve-fitting yielded estimated IC_{50} values; in 3D monoculture (Figure 6C), the estimated IC_{50} for cisplatin was 10.7 µM for UT-

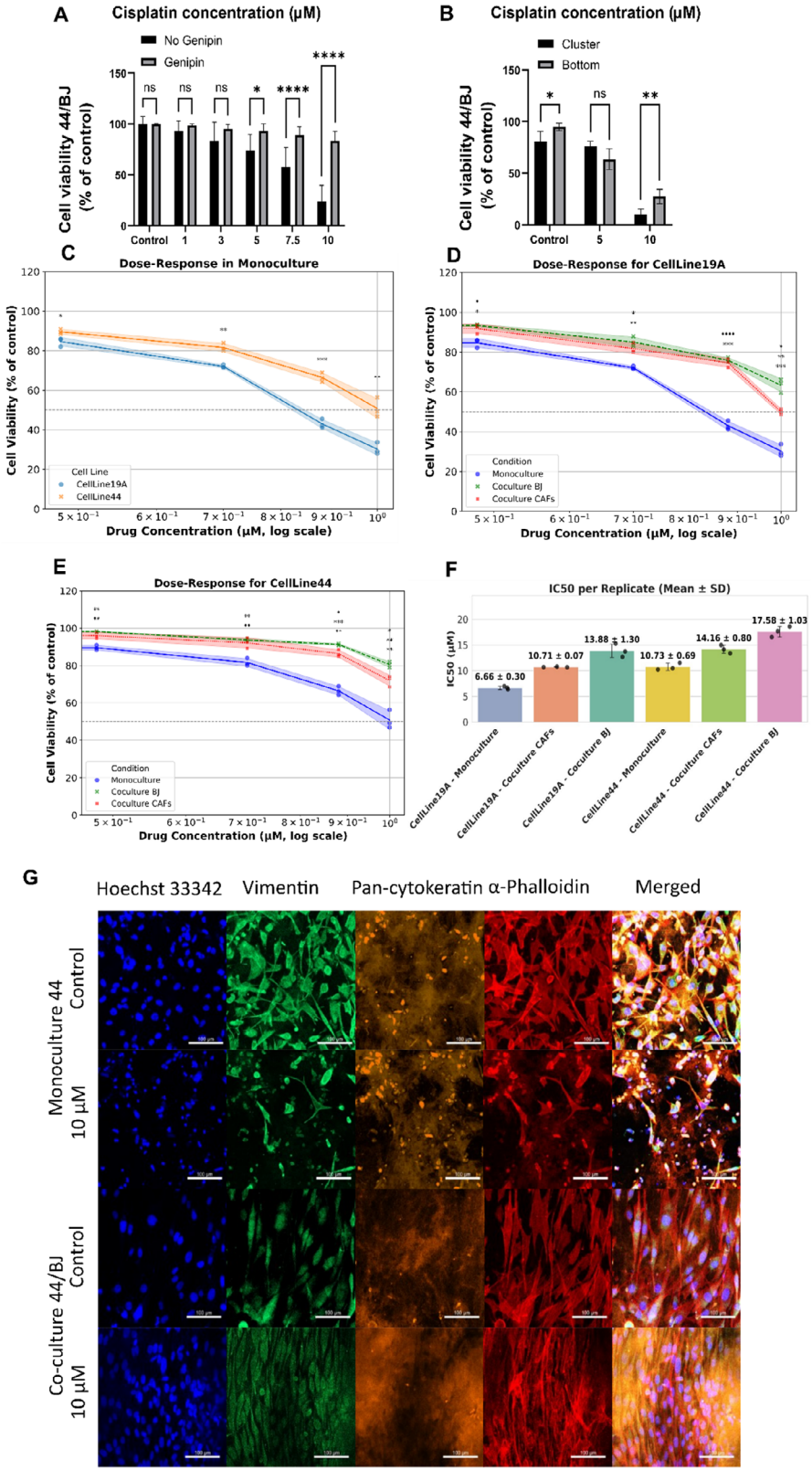

FIGURE 6 | Genipin-crosslinked hydrogel microfluidic model recapitulates drug sensitivity and stromal-mediated chemoprotection in 3D tumor co-cultures. (A) Cisplatin dose–response in UT-SCC-19A and UT-SCC-44 tumor–fibroblast co-cultures embedded in native (non-Genipin-crosslinked) vs. Genipin-crosslinked hydrogels. (B) Comparison of drug sensitivity in native hydrogels between cells adhered to the chip surface and cells retained within the hydrogel matrix. (C–E) Dose–response curves for UT-SCC-19A (C) and UT-SCC-44 (E) in monoculture, co-culture with BJ fibroblasts, and co-culture with patient-derived CAFs. Each marker represents one biological replicate (independently seeded chip; $n = 3$ per condition). For each chip, one to several non-overlapping fields of view were acquired and averaged to generate a single chip-level value used for statistical analysis. Viability is expressed as a percentage of the matched vehicle control (control = 100%) and plotted against log-transformed cisplatin concentrations. (F) Summary

SCC-44 and 6.7 μM for UT-SCC-19A, respectively. For UT-SCC-19A cells (Figure 6D), the IC_{50} observed for cisplatin increased from 6.66 μM observed in monoculture (blue line) to 13.9 μM in co-culture with normal fibroblasts (BJ, green line), and to 10.7 μM in co-culture with CAFs (red line). For UT-SCC-44 cells (Figure 6E), the IC_{50} rose from 10.7 μM observed in monoculture (blue line) to 17.6 μM in co-culture with normal fibroblasts (BJ, green line) and 14.2 μM with CAFs (red line). Crucially, primary patient-derived CAFs isolated from patient-derived HNSCC tissue further enhanced the clinical relevance of the model, although in these experiments, they did not enhance drug tolerance beyond BJ cell levels (summarized in Figure 6F). These primary CAFs maintained donor-specific heterogeneity and induced variable protective effects, underscoring the role of stromal context in modulating treatment response. Immunofluorescence confirmed preserved tumor tissue-like architecture and viability at 10 μM (Figure 6G), indicating significant chemoprotection mediated by stromal cells.

These findings establish hydrogel microfluidic models generated by Genipin-crosslinking of the matrix as clinically relevant platforms for drug profiling in tumor-stroma co-cultures. The system supports long-term 3D viability, preserves EMT- and stroma-linked phenotypes, and enables multiparametric readouts—including morphometric analysis (Figure S5). Incorporation of patient-derived CAFs adds biological fidelity, making this a promising tool for preclinical testing and precision oncology.

4 | Discussion

Recreating the tumor–stroma interface in vitro remains a central challenge in cancer biology and therapeutic development. The TME is not a passive scaffold but an active driver of cancer progression, therapeutic resistance, and metastasis [12, 13]. In desmoplastic tumors such as HNSCC, CAFs and their remodeling of the ECM play a key role in shaping tumor behavior [14, 15]. Yet most in vitro systems—including spheroids, organoids, and tumor-on-chip platforms—either completely omit the highly dynamic fibroblasts or fail to support long-term, spatially organized tumor–stroma interactions within a structurally stable ECM [45–47].

Here, we introduce a multifunctional hydrogel-based microfluidic platform that enables sustained, spatially resolved tumor–fibroblast co-culture by addressing matrix contraction and hydrogel detachment—two long-standing barriers in 3D co-culture systems. Rheology and spectroscopy together clarify how our approach stabilizes the matrix. FTIR confirms covalent Genipin–amine crosslinks while also indicating retention of reactive —OH/—NH_2 groups, and time- and frequency-resolved rheology documents progressive network maturation, supported by other studies [48, 49], which persist over extended culture periods.

Although the absolute increase in bulk stiffness was moderate, the combination of ongoing covalent maturation and preserved surface-reactive groups likely underpins the improved resistance to fibroblast-mediated contraction and device delamination. These retained functional groups enable covalent bonding to APTES-functionalized PDMS and glass, so the stabilization arises from a synergy of internal (Genipin-mediated) reinforcement and durable surface anchoring rather than from dramatic bulk stiffening alone.

Our design (Figures 1A–C and 2F) integrates a dual ECM stabilization strategy, combining Genipin-mediated crosslinking with APTES-based silanization, to resist fibroblast-induced contraction while maintaining robust hydrogel anchorage to both PDMS and glass substrates over extended durations [50, 51]. This allows direct tumor–fibroblast co-culture within a shared 3D ECM that better replicates in vivo architecture, an approach rarely utilized in vitro.

Previous implementations of APTES and Genipin crosslinking have focused on pericardial patches, AFM probes, biosensor surfaces, or simple cell adhesion assays [24–27]; our data extend these applications by demonstrating utility in complex tumor-fibroblast systems that exhibit active matrix remodeling. Remaining limitations include potential effects of crosslinking on matrix ligand presentation [52] and inter-batch variability of biological ECM components [53]; future work will profile ligand accessibility, further tune crosslink density for different tumor types, and benchmark predictive power against patient responses.

Matrix stabilization is critical in fibroblast-rich cultures, particularly under microfluidic conditions, where steep oxygen and

of IC_{50} values calculated from chip-level normalized viability using nonlinear regression to a four-parameter Hill equation (4PL) in Python (Python 3.11.11, Google Colaboratory) with 95% confidence intervals. Bars indicate the mean IC_{50} ± SD (μM). Individual on-chip replicate level IC_{50} ($n = 3$) are shown as black dots. The IC_{50} values presented are exploratory estimates from four-parameter curve fitting. For conditions where the dose–response curve does not reach 50% inhibition within the tested range (1–10 μM), fitted values represent extrapolations beyond the experimental data and should be interpreted with caution. Comparative viability at 5 and 10 μM (Figure 6C–E) is the primary basis for assessing differential drug sensitivity across conditions. (G) Representative immunofluorescence images of UT-SCC-44 in 3D monoculture and BJ co-culture following 4 days of Cisplatin treatment. These panels show high-magnification regions of interest selected to illustrate morphology and cytoskeletal responses and are not intended to represent whole-chip cell density. Samples were stained for Vimentin (mesenchymal marker), Pan-cytokeratin (epithelial marker), Phalloidin (F-actin), and Hoechst 33342 (nuclei). Z-projected images acquired using a 10× objective on super-resolution microscopy. Scale bar = 100 μm. Statistical analysis: All inferential statistics were performed on chip-level values (chip = independent biological replicate). For panels (A) and (B), dose–response comparisons were analyzed using two-way ANOVA (two-sided) in GraphPad Prism 9 (v9.5.1) with Sidak's post-hoc test for multiple comparisons. For panels (C–E), at each cisplatin concentration, comparisons between two groups (cell lines or culture conditions) were performed using Welch's *t*-tests (two-sided, independent samples). Normality was assessed using Shapiro–Wilk test where applicable ($n \geq 3$). Exact *p*-values are reported in the figure or figure legend. Significance: *$p < 0.05$; **$p < 0.01$; ***$p < 0.001$; ****$p < 0.0001$.

nutrient gradients drive fibroblast activation and contractility [54, 55]. This commonly leads to ECM contraction, hydrogel delamination, and tissue necrosis—especially in native or non-stabilized matrices (Figures 3 and 4) [56–58]. Consequently, many co-culture systems are limited to short-term durations (<7 days), often with structural collapse and compromised viability [59–61]. Our platform overcomes these limitations, supporting long-term culture (≥10 days) while preserving tissue morphology, spatial organization, and phenotype-resolved drug response.

The ECM formulation—a blend of Mat/COL/HA —was empirically optimized to balance bioactivity and structural resilience. COL enables fibroblast-driven remodeling [36, 62]; HA contributes to increased viscoelasticity and hydration [63, 64]; and Matrigel proved essential to resist fibroblast-mediated contraction in COL/HA-only matrices, likely due to its laminin-rich composition. In addition, Matrigel promoted the spontaneous self-organization of tumor and stromal cells into tissue-like structures [65–67]. Importantly, a systematic parametric study varying individual components would provide deeper mechanistic insight into their specific contributions. For example, COL concentration effects on stiffness and fibroblast-driven remodeling [68, 69], HA concentration effects on matrix hydration/viscoelasticity [70] and fibroblast phenotype [71], and Matrigel concentration effects on composite structural integrity, contractility, and epithelial organization [72–75]. This represents an important direction for future work.

To counteract matrix contraction, existing strategies typically involve trade-offs between structural stability, cytocompatibility, and imaging access. For example:

- Riboflavin/UVA photoinitiation offers rapid crosslinking but risks phototoxicity [76].
- Glutaraldehyde, while mechanically robust, significantly impairs fibroblast viability due to its toxicity, even at low concentrations (0.01% reduces viability by ~70%) [77].
- PEG-based and enzymatic crosslinkers are more biocompatible but often require prolonged curing and can reduce optical transparency [78].
- Mechanical constraints like microposts (micropillars) or confinement chambers prevent contraction but hinder perfusion and imaging [79].
- Synthetic ECMs offer tunability but often lack essential bioactivity or require functionalization to support CAF remodeling [80].

Surface coatings such as polysaccharide glue and polydopamine have been used to improve hydrogel adhesion via electrostatic or covalent interactions [81, 82]. However, neither method has been quantitatively validated against the strong fibroblast-mediated contraction in tumor-fibroblast microfluidic co-cultures. In contrast, APTES-based silanization forms covalent bonds with both the ECM scaffold and the device surface, providing durable anchorage that maintains structural integrity under sustained fibroblast-generated contractile stress.

We do not intend to claim intrinsic superiority of microfluidic systems over all well-plate-based approaches. Rather, the specific combination of active matrix contraction, ECM remodeling under fibroblast-generated forces, and long-term tumor–fibroblast co-culture that is central to our biological questions specifically benefits from confined geometry and covalent surface anchoring—features that proved difficult to maintain in standard well-plate 3D formats under our experimental conditions. In parallel, we evaluated the same tumor–fibroblast co-cultures in commonly used 96-well 3D formats, including Mat/COL/HA domes and "sandwich" models set up in angiogenesis plates (Figure S6). In our hands, both approaches exhibited rapid gel contraction, adhesion to the substrate, and loss of 3D architecture within a few days. While the substrate functionalization and crosslinking strategy described here could in principle be translated to well-plate formats, a direct quantitative comparison between microfluidic chips and static wells was not pursued, as it would introduce multiple confounding variables (geometry, gel volume, surface-to-volume ratio, diffusion dynamics). Systematic cross-format benchmarking, therefore, remains an important direction for future studies. Our dual-stabilization strategy addresses these challenges comprehensively. Genipin, a naturally derived crosslinker, covalently bonds primary amine groups in ECM proteins while maintaining good cytocompatibility [83]. Combined with APTES surface anchoring, this approach preserves structural integrity, optical clarity, and long-term viability (>85% over ≥10 days), while maintaining imaging accessibility and minimizing disruption to cell behavior.

However, matrix crosslinking can alter small-molecule transport by reducing pore size and increasing network tortuosity, effects that have been reported across multiple hydrogel systems [84–86]. In addition, an important limitation of our live/dead assay is the inability to distinguish tumor cell vs. fibroblast viability. Given the inherent chemoresistance of fibroblasts, the overall viability signal likely reflects contributions from both populations. Future iterations should incorporate cell-type-specific fluorescent labeling (e.g., tdTomato tumor cells) to deconvolve these responses. That said, several features of our dataset argue that altered diffusion alone does not fully account for the observed stromal protection: (i) the principal comparisons are made within the same matrix condition (monoculture vs. co-culture), (ii) patient-derived CAFs confer protection in native gels (Figure S7), and (iii) imaging demonstrates preservation of pan-cytokeratin^{+} tumor structures under co-culture at relevant doses (Figure S5).

The stabilized hydrogel system enables non-destructive, time-resolved analysis under perfused conditions. Phenotypic metrics (Figure 5 and Figure S5), such as surface-area-to-volume ratios and bounding box dimensions, enable real-time tracking of morphodynamic changes, cytotoxic responses, and ECM remodeling, capturing functional changes not detectable with viability assays alone.

This structural stability is essential for preserving tumor phenotype and therapeutic relevance. HNSCC microtissues maintained subtype-specific architecture, proliferation, and viability within the stabilized ECM (Figures 3 and 4). Native matrices, in contrast, collapsed rapidly, causing spatial disorganization—see comparison in Figure S6. Notably, fibroblast/CAF co-culture significantly reduced Cisplatin sensitivity (Figure 6C–F), which is consistent with in vivo stromal protection but rarely recapitulated in vitro [87]. Given the focus on physiologically observable concentra-

tions, systematic extension of the dose–response range will be an important next step to further delineate the pharmacodynamic landscape of this platform. Subtype-specific responses were retained: the epithelial UT-SCC-19A remained more sensitive than the mesenchymal-like UT-SCC-44, reflecting its likely EMT-associated resistance (Figure S2) [88]. We emphasize that the model does not aim to recapitulate full terminal squamous epithelial differentiation. We did not assess terminal differentiation markers (e.g., involucrin or filaggrin), and the observed morphological features and pan-cytokeratin patterns should therefore be interpreted as evidence of tissue-like spatial organization rather than confirmed epithelial stratification or differentiation in the molecular sense.

A further limitation is that we did not perform a comprehensive functional CAF conversion analysis of BJ fibroblasts within our microfluidic platform. The rationale for using BJ fibroblasts rests on published evidence that normal fibroblasts rapidly acquire CAF-like phenotypes upon co-culture with cancer cells; however, this transition was not directly validated in our specific system using markers of CAF activation (e.g., αSMA induction, FAP expression, or secretome profiling). Future work should directly characterize the BJ fibroblast activation state following co-culture in our microfluidic setting.

Beyond pharmacologic testing, the platform has strong translational potential. Its compatibility with hydrostatic flow and low input requirements makes it suitable for patient-derived samples and multiplexed assays [89]. By preserving stromal dynamics and spatial organization, the system models key features of the TME increasingly recognized as modulators of drug response [90].

The microfluidic format further benefits our approach by reducing reagent and ECM consumption (≈5 µL per chip vs. ≈40 µL per 96-well "sandwich" model), enabling parallelized chambers for internal replicates, and producing shallow, uniform gels that improve antibody penetration and z-stack reproducibility for automated high-content imaging. Lower gel volumes also permit more controlled, rapid equilibration of drug dosing and reduce inter-well geometric variability, improving assay reproducibility [91]. We intentionally used static media exchange (24–48 h) rather than continuous perfusion because (i) interstitial transport in solid tissues is slow and diffusion-dominated, making intermittent exchange biologically relevant [92]; and (ii) pilot tests showed that transient bubbles and flow transients can induce local delamination or collapse of delicate gels, introducing a confounding structural variable. Finally, (iii) static operation simplifies imaging and quantitative analysis by avoiding flow-induced focal drift and transient advective concentration spikes, helping ensure that our readouts reflect the stabilization strategy rather than flow artifacts [93].

Looking forward, this platform offers a versatile foundation for integrating immune components and studying tumor–stroma–immune interactions. Dense or contracted ECMs are known to limit immune infiltration, particularly T cells [94]. The structural stability, and optical accessibility of our system enable quantitative studies of these transport barriers. With further development, the model could be extended to stromal-rich malignancies such as pancreatic, colorectal, or triple-negative breast cancers, and paired with high-content imaging and machine learning for morphodynamic/phenotypic analysis [95, 96].

In summary, we present a materials-engineered strategy that bridges structural robustness and biological complexity to support long-term, spatially organized tumor–CAF co-culture in microfluidic conditions. This platform provides a structurally stable, pharmacologically informative, and translationally relevant model for cancer research, with broad applicability in precision oncology.

5 | Conclusion

In summary, we present a modular microfluidic platform that enables long-term 3D co-culture of tumor cells and CAFs within a structurally stabilized, bioactive ECM. By combining APTES-mediated surface functionalization with Genipin crosslinking, the system prevents matrix detachment and contraction—common limitations in COL-rich microenvironments – while maintaining high viability, spatial organization, and phenotypic heterogeneity over 10 days. Time- and frequency-resolved rheology confirmed progressive network maturation in Genipin-crosslinked hydrogels, with increases in storage modulus (G′) and enhanced resistance to large-strain deformation, consistent with FTIR evidence for covalent crosslinks and residual reactive groups available for surface anchoring. These features enabled the formation of self-organized tumor microtissues with >85% viability and a two-fold increase in Ki67 expression, along with reproducible drug response profiles.

The platform supports high-content, semi-automated morphometric analysis and multiplexed drug testing, offering a versatile toolkit for functional profiling of patient-specific tumor-stroma dynamics. By integrating rational ECM design, surface engineering, and progressive hydrogel network reinforcement, this system resolves key structural and biochemical constraints in microfluidic culture systems.

By capturing stromal-mediated drug resistance and incorporating patient-derived CAFs, it provides a proof-of-concept model for clinical translation, with potential for fully autologous components and on-chip analytics in future iterations.

Author Contributions

R.K.E. contributed to the microfluidic chip design and developed the dual APTES–Genipin functionalization strategy. The scientific concept and study design were developed collaboratively by R.K.E., Doriane Le Manach (D.L.M.), and Matthias Nees (M.N.), with M.N. contributing particularly to translational framing and scientific supervision. D.L.M. led the biological implementation strategy, including the development of tumor–stroma co-culture models, experimental validation, and data analysis. R.K.E. developed and fabricated microfluidic chips. D.L.M. performed cell culture, hydrogel experiments, immunofluorescence staining, confocal imaging, drug screening assays, viability analyses, image processing, and quantitative morphometric analysis. E.R. contributed to the isolation of primary cancer-associated fibroblasts (CAFs), the implementation of hyaluronic acid (HA) incorporation protocols in hydrogel preparation, and the characterization of materials by FTIR-ATR. D.L.M. conducted data interpretation. D.L.M. wrote the manuscript with substantial support

from M.N. and revisions from all co-authors. Project supervision was provided by D.L.M. and MN, with co-supervision by R.K.E. and P.N. Funding for the project was acquired by M.N., P.N., D.L.M., and R.K.E. All authors reviewed and approved the final manuscript.

Acknowledgements

We sincerely thank Michel Cloitre, from Molecular, Macromolecular Chemistry and Materials, ESPCI Paris, CNRS, PSL Research University, for his generous support with rheology experiments, analysis, figure design, and helpful discussions throughout the preparation of this study. We would like to thank Dr. Sebastian Janik from the Department of Biophysics, Institute of Physics, Maria Curie-Skłodowska University (Lublin, Poland), who is led by Prof. Dr. hab. Wiesław I. Gruszecki, who performed super-resolution microscopy purchased with financial support from the Ministry of Science and Higher Education under Grant Number. 7374/IA/SP/2023, which was awarded to Prof. Dr. hab. Rafał Luchowski. We also thank Dr. Hab. Justyna Widomska from the Biophysics Department of the Medical University (Lublin, Poland) for allowing us to use the Nicolet 6700 (Thermo Scientific) for FTIR-ATR spectroscopic measurements. Finally, we thank Lindsey Marshall and Patrice Mascalchi from Leica Microsystems for their assistance with AIVIA.

Funding

This research was funded by the Polish National Science Centre (NCN): UMO-2020/37/B/NZ4/03920, and DEC-2021/41/B/NZ7/03786, the EMBO Scientific Exchange Grant (no. 10698), the Polish National Agency for Academic Exchange (NAWA): PPI/APM/2019/1/00089/U/00001, the Jane & Aatos Erkko Foundation, project "Matrix Matters", and the Academy of Finland "Phenotypic Screening for Cancer Drug Discovery"/Consortium: PESCADoR (309372). This work was also supported by Institut Pierre-Gilles de Gennes ANR-10-EQPX-34, EU Horizon 2020 Grant ERC PoC (101100823), and the PSL QLife initiative.

Conflicts of Interest

The authors D.L.M., R.K.E., and M.N. are co-inventors on a patent related to the cell culture platform described in this work. R.K.E. was an employee of UMR CNRS-ESPCI 8231 Chimie Biologie Innovation, PSL University at the time of the study design and experimental studies.

Data Availability Statement

The data that support the findings of this study and the Python scripts are available from the corresponding authors upon reasonable request.

References

1. M. Gormley, G. Creaney, A. Schache, K. Ingarfield, and D. I. Conway, "Reviewing the Epidemiology of Head and Neck Cancer: Definitions, Trends and Risk Factors," *British Dental Journal* 233, no. 9 (2022): 780–786, https://doi.org/10.1038/s41415-022-5166-x.

2. H. Picon and A. K. Guddati, "Cancer Stem Cells in Head and Neck Cancer," *American Journal of Stem Cells* 10, no. 3 (2021): 28-35.

3. E. Alsahafi, K. Begg, I. Amelio, et al., "Clinical Update on Head and Neck Cancer: Molecular Biology and Ongoing Challenges," *Cell death & disease* 10, no. 8 (2019): 540, https://doi.org/10.1038/s41419-019-1769-9.

4. X. Li, C. Shao, Y. Shi, and W. Han, "Lessons Learned from the Blockade of Immune Checkpoints in Cancer Immunotherapy," *Journal of Hematology & Oncology* 11, no. 1 (2018): 31, https://doi.org/10.1186/s13045-018-0578-4.

5. C. Jubelin, J. Muñoz-Garcia, L. Griscom, et al., "Three-dimensional in Vitro Culture Models in Oncology Research," *Cell & Bioscience* 12, no. 1 (2022): 155, https://doi.org/10.1186/s13578-022-00887-3.

6. I. Dagogo-Jack and A. T. Shaw, "Tumour Heterogeneity and Resistance to Cancer Therapies," *Nature Reviews Clinical Oncology* 15, no. 2 (2018): 81-94, https://doi.org/10.1038/nrclinonc.2017.166.

7. T. Lepikhova, P. R. Karhemo, R. Louhimo, et al., "Drug-Sensitivity Screening and Genomic Characterization of 45 HPV-Negative Head and Neck Carcinoma Cell Lines for Nov.El Biomarkers of Drug Efficacy," *Molecular Cancer Therapeutics* 17, no. 9 (2018): 2060–2071, https://doi.org/10.1158/1535-7163.MCT-17-0733.

8. L. C. Bahlmann, L. J. Smith, and M. S. Shoichet, "Designer Biomaterials to Model Cancer Cell Invasion in Vitro: Predictive Tools or Just Pretty Pictures?," *Advanced Functional Materials* 30, no. 16 (2020): 1909032, https://doi.org/10.1002/adfm.201909032.

9. P. Chaves, M. Garrido, J. Oliver, E. Pérez-Ruiz, I. Barragan, and A. Rueda-Domínguez, "Preclinical Models in Head and Neck Squamous Cell Carcinoma," *British Journal of Cancer* 128, no. 10 (2023): 1819–1827, https://doi.org/10.1038/s41416-023-02186-1.

10. A. Elmusrati, J. Wang, and C. Y. Wang, "Tumor Microenvironment and Immune Evasion in Head and Neck Squamous Cell Carcinoma," *International Journal of Oral Science* 13, no. 1 (2021): 24, https://doi.org/10.1038/s41368-021-00131-7.

11. S. V. Puram, I. Tirosh, A. S. Parikh, et al., "Single-cell Transcriptomic Analysis of Primary and Metastatic Tumor Ecosystems in Head and Neck Cancer," *Cell* 171, no. 7 (2017): 1611.

12. G. P. M. Jr, Z. X, and D. Zheng, "Molecular Features of Cancer-associated Fibroblast Subtypes and Their Implication on Cancer Pathogenesis, Prognosis, and Immunotherapy Resistance," *Clinical Cancer Research* 27, no. 9 (2021): 2636–2647, https://doi.org/10.1158/1078-0432.CCR-20-4226.

13. K. Punovuori, F. Bertillot, Y. A. Miroshnikova, et al., "Multiparameter Imaging Reveals Clinically Relevant Cancer Cell-stroma Interaction Dynamics in Head and Neck Cancer," *Cell* 187, no. 25 (2024): 7267–7284e20, https://doi.org/10.1016/j.cell.2024.09.046.

14. M. R. Junttila and F. J. de Sauvage, "Influence of Tumour Microenvironment Heterogeneity on Therapeutic Response," *Nature* 501, no. 7467 (2013): 346–354, https://doi.org/10.1038/nature12626.

15. X. Li, C. González-Maroto, and M. Tavassoli, "Crosstalk between CAFs and Tumour Cells in Head and Neck Cancer," *Cell Death Discovery* 10, no. 1 (2024): 303, https://doi.org/10.1038/s41420-024-02053-9.

16. C. S. Szot, C. F. Buchanan, J. W. Freeman, and M. N. Rylander, "3D in Vitro Bioengineered Tumors Based on Collagen I Hydrogels," *Biomaterials* 32, no. 31 (2011): 7905–7912, https://doi.org/10.1016/j.biomaterials.2011.07.001.

17. A. ID, "Collagen Hydrogel in Drug Delivery and Tissue Engineering," in *Biomaterial-based Hydrogels: Therapeutics Carrier and Tissue Regeneration*, ed. S. Jana, (Springer Nature, 2024), 199–243, https://doi.org/10.1007/978-981-99-8826-6_8.

18. P. Monteiro, D. Remy, E. Lemerle, et al., "A Mechanosensitive Caveolae–Invadosome Interplay Drives Matrix Remodelling for Cancer Cell Invasion," *Nature Cell Biology* 25, no. 12 (2023): 1787–1803, https://doi.org/10.1038/s41556-023-01272-z.

19. B. F. L. Lai, R. X. Z. Lu, Y. Hu, et al., "Recapitulating Pancreatic Tumor Microenvironment through Synergistic Use of Patient Organoids and Organ-on-a-Chip Vasculature," *Advanced Functional Materials* 30, no. 48 (2020): 2000545, https://doi.org/10.1002/adfm.202000545.

20. J. J. F. Sleeboom, G. S. van Tienderen, K. Schenke-Layland, L. J. W. van der Laan, A. A. Khalil, and M. M. A. Verstegen, "The Extracellular Matrix as Hallmark of Cancer and Metastasis: from Biomechanics to Therapeutic Targets," *Science Translational Medicine* 16, no. 728 (2024): adg3840, https://doi.org/10.1126/scitranslmed.adg3840.

21. M. R. Zanotelli, J. P. Miller, W. Wang, et al., "Tension Directs Cancer Cell Migration over fiber Alignment through Energy Minimization," *Biomaterials* 311 (2024): 122682, https://doi.org/10.1016/j.biomaterials.2024.122682.

22. F. Grinnell and W. M. Petroll, "Cell Motility and Mechanics in Three-dimensional Collagen Matrices," *Annual Review of Cell and Developmental Biology* 26 (2010): 335–361, https://doi.org/10.1146/annurev.cellbio.042308.113318.

23. J. Winkler, A. Abisoye-Ogunniyan, K. J. Metcalf, and Z. Werb, "Concepts of Extracellular Matrix Remodeling in Tumour Progression and Metastasis," *Nature Communications* 11, no. 1 (2020): 5120, https://doi.org/10.1038/s41467-020-18794-x.

24. M. Sypabekova, J. Kleiss, A. Hagemann, et al., "Improvement of the Optical Cavity-based Biosensor's Limit of Detection Using Optimal 3-aminopropyltriethoxysilane Process," *Scientific Reports* 15, no. 1 (2025): 7739, https://doi.org/10.1038/s41598-025-92151-0.

25. A. Siddique, T. Meckel, R. W. Stark, and S. Narayan, "Improved Cell Adhesion under Shear Stress in PDMS Microfluidic Devices," *Colloids and Surfaces B: Biointerfaces* 150 (2017): 456–464, https://doi.org/10.1016/j.colsurfb.2016.11.011.

26. J. S. Yoo, Y. J. Kim, S. H. Kim, and S. H. Choi, "Study on Genipin: A New Alternative Natural Crosslinking Agent for Fixing Heterograft Tissue," *The Korean Journal of Thoracic and Cardiovascular Surgery* 44, no. 3 (2011): 197–207, https://doi.org/10.5090/kjtcs.2011.44.3.197.

27. H. Holuigue, L. Nacci, P. Di Chiaro, et al., "Native Extracellular Matrix Probes to Target Patient- and Tissue-specific Cell–microenvironment Interactions by Force Spectroscopy," *Nanoscale* 15, no. 37 (2023): 15382–15395, https://doi.org/10.1039/D3NR01568H.

28. J. M. Ayuso, M. Virumbrales-Muñoz, J. M. Lang, and D. J. Beebe, "A Role for Microfluidic Systems in Precision Medicine," *Nature Communications* 13, no. 1 (2022): 3086, https://doi.org/10.1038/s41467-022-30384-7.

29. M. Filippi, T. Buchner, O. Yasa, S. Weirich, and R. K. Katzschmann, "Microfluidic Tissue Engineering and Bio-Actuation," *Advanced Materials* 34, no. 23 (2022): 2108427, https://doi.org/10.1002/adma.202108427.

30. A. Bhusal, S. Yogeshwaran, H. Goodarzi Hosseinabadi, B. Cecen, and A. K. Miri, "Microfluidics for High Throughput Screening of Biological Agents and Therapeutics," *Biomedical Materials & Devices* 3 (2024): 93–107, https://doi.org/10.1007/s44174-024-00169-1.

31. A. Enders, A. Grünberger, and J. Bahnemann, "Towards Small Scale: Overview and Applications of Microfluidics in Biotechnology," *Molecular Biotechnology* 66, no. 3 (2024): 365–377, https://doi.org/10.1007/s12033-022-00626-6.

32. A. Anameriç, A. Czerwonka, and M. Nees, "Optimization of a Three-Dimensional Culturing Method for Assessing the Impact of Cisplatin on Notch Signaling in Head and Neck Squamous Cell Carcinoma (HNSCC)," *Cancers* 15, no. 22 (2023): 22, https://doi.org/10.3390/cancers15225320.

33. S. Afshan, Y. G. Kim, J. Mattsson, et al., "Targeting the Cancer Cells and Cancer-Associated Fibroblasts with next-Generation FGFR Inhibitors in Prostate Cancer co-Culture Models," *Cancer Medicine* 13, no. 18 (2024): 70240, https://doi.org/10.1002/cam4.70240.

34. K. Výborný, J. Vallová, Z. Kočí, et al., "Genipin and EDC Crosslinking of Extracellular Matrix Hydrogel Derived from human Umbilical Cord for Neural Tissue Repair," *Scientific Reports* 9, no. 1 (2019): 10674, https://doi.org/10.1038/s41598-019-47059-x.

35. Aivia 14-Deeper Spatial Insights Powered by AI [accessed 9 September 2024]. Disponible sur: https://www.aivia-software.com/aivia14.

36. M. Åkerfelt, N. Bayramoglu, S. Robinson, et al., "Automated Tracking of Tumor-stroma Morphology in Microtissues Identifies Functional Targets within the Tumor Microenvironment for Therapeutic Intervention," *Oncotarget* 6, no. 30 (2015): 30035–30056, https://doi.org/10.18632/oncotarget.5046.

37. A. Anameriç, E. Reszczyńska, T. Stankiewicz, A. Andrzejczak, A. Stepulak, and M. Nees, "A Patient-Derived Scaffold-Based 3D Culture Platform for Head and Neck Cancer: Preserving Tumor Heterogeneity for Personalized Drug Testing," *Cells* 14, no. 19 (2025): 1543, https://doi.org/10.3390/cells14191543.

38. H. G. Sundararaghavan, G. A. Monteiro, N. A. Lapin, Y. J. Chabal, J. R. Miksan, and D. I. Shreiber, "Genipin-induced Changes in Collagen Gels: Correlation of Mechanical Properties to Fluorescence," *Journal of Biomedical Materials Research Part A* 87A, no. 2 (2008): 308-320, https://doi.org/10.1002/jbm.a.31715.

39. V. M. Perez-Puyana, E. Cortés-Triviño, M. Jiménez-Rosado, A. Romero, and I. Martínez, "Pea Protein-Based Bioplastics Crosslinked with Genipin: Analysis of the Crosslinking Evolution," *Journal of Polymers and the Environment* 32, no. 1 (2024): 31-44, https://doi.org/10.1007/s10924-023-02973-0.

40. K. Madhavan, D. Belchenko, and W. Tan, "Roles of Genipin Crosslinking and Biomolecule Conditioning in Collagen-Based Biopolymer: Potential for Vascular media Regeneration," *Journal of Biomedical Materials Research Part A* 97A, no. 1 (2011): 16-26, https://doi.org/10.1002/jbm.a.33006.

41. L. K. Tamm and S. A. Tatulian, "Infrared Spectroscopy of Proteins and Peptides in Lipid Bilayers," *Quarterly Reviews of Biophysics* 30, no. 4 (1997): 365-429, https://doi.org/10.1017/s0033583597003375.

42. M. Bues-Charbit, J. C. Gentet, J. L. Bernard, V. Breant, J. P. Cano, and C. Raybaud, "Continuous Infusion of High-Dose Cisplatin in Children: Pharmacokinetics of Free and Total Platinum," *European Journal of Cancer and Clinical Oncology* 23, no. 11 (1987): 1649–1652, https://doi.org/10.1016/0277-5379(87)90444-5.

43. C. Dominici, F. Petrucci, S. Caroli, A. Alimonti, A. Clerico, and M. A. Castello, "A Pharmacokinetic Study of High-Dose Continuous Infusion Cisplatin in Children with Solid Tumors," *Journal of Clinical Oncology* 7, no. 1 (1989): 100–107, https://doi.org/10.1200/JCO.1989.7.1.100.

44. L. A. W. de Jong, M. Lambert, N. P. van Erp, L. de Vries, E. Chatelut, and P. B. Ottevanger, "Systemic Exposure to Cisplatin and Paclitaxel after Intraperitoneal Chemotherapy in Ovarian Cancer," *Cancer Chemotherapy and Pharmacology* 91, no. 3 (2023): 247-256, https://doi.org/10.1007/s00280-023-04512-z.

45. M. Chung, J. Ahn, K. Son, S. Kim, and N. L. Jeon, "Biomimetic Model of Tumor Microenvironment on Microfluidic Platform," *Advanced Healthcare Materials* 6, no. 15 (2017): 1700196, https://doi.org/10.1002/adhm.201700196.

46. V. Sgarminato, S. L. Marasso, M. Cocuzza, et al., "PDAC-on-chip for in Vitro Modeling of Stromal and Pancreatic Cancer Cell Crosstalk," *Biomaterials Science* 11, no. 1 (2022): 208-224, https://doi.org/10.1039/D2BM00881E.

47. S. Y. Jeong, J. H. Lee, Y. Shin, S. Chung, and H. J. Kuh, "Co-Culture of Tumor Spheroids and Fibroblasts in a Collagen Matrix-Incorporated Microfluidic Chip Mimics Reciprocal Activation in Solid Tumor Microenvironment," *PLoS ONE* 11, no. 7 (2016): 0159013, https://doi.org/10.1371/journal.pone.0159013.

48. Z. Wang, H. Liu, W. Luo, et al., "Regeneration of Skeletal System with Genipin Crosslinked Biomaterials," *Journal of Tissue Engineering* 11 (2020): 2041731420974861, https://doi.org/10.1177/2041731420974861.

49. S. Elder, A. Pinheiro, C. Young, P. Smith, and E. Wright, "Evaluation of Genipin for Stabilization of Decellularized Porcine Cartilage," *Journal of Orthopaedic Research* 35, no. 9 (2017): 1949-1957, https://doi.org/10.1002/jor.23483.

50. A. Al-Ali, W. Waheed, F. Dawaymeh, N. Alamoodi, and A. Alazzam, "A Surface Treatment Method for Improving the Attachment of PDMS: Acoustofluidics as a Case Study," *Science Reports* 13, no. 1 (2023): 18141, https://doi.org/10.1038/s41598-023-45429-0.

51. P. J. Wipff, H. Majd, C. Acharya, L. Buscemi, J. J. Meister, and B. Hinz, "The Covalent Attachment of Adhesion Molecules to Silicone Membranes for Cell Stretching Applications," *Biomaterials* 30, no. 9 (2009): 1781-1789, https://doi.org/10.1016/j.biomaterials.2008.12.022.

52. N. Davidenko, C. F. Schuster, D. V. Bax, et al., "Evaluation of Cell Binding to Collagen and Gelatin: a Study of the Effect of 2D and 3D Architecture and Surface Chemistry," *Journal of Materials Science:*

Materials in Medicine 27, no. 10 (2016): 148, https://doi.org/10.1007/s10856-016-5763-9.

53. E. A. Aisenbrey and W. L. Murphy, "Synthetic Alternatives to Matrigel," *Nature Reviews Materials* 5, no. 7 (2020): 539-551, https://doi.org/10.1038/s41578-020-0199-8.

54. C. P. Ng, B. Hinz, and M. A. Swartz, "Interstitial Fluid Flow Induces Myofibroblast Differentiation and Collagen Alignment in Vitro," *Journal of Cell Science* 118, no. 20 (2005): 4731-4739, https://doi.org/10.1242/jcs.02605.

55. W. Sun, Y. Chen, Y. Wang, et al., "Interaction Study of Cancer Cells and Fibroblasts on a Spatially Confined Oxygen Gradient Microfluidic Chip to Investigate the Tumor Microenvironment," *Analyst* 143, no. 22 (2018): 5431-5437, https://doi.org/10.1039/C8AN01216D.

56. C. J. Gommes, T. Louis, I. Bourgot, A. Noël, S. Blacher, and E. Maquoi, "Remodeling of the Fibre-Aggregate Structure of Collagen Gels by Cancer-associated Fibroblasts: a Time-resolved Grey-tone Image Analysis Based on Stochastic Modelling," *Front Immunol* 13 (2023), https://doi.org/10.3389/fimmu.2022.988502.

57. J. A. McKee, E. A. Olsen, G. Wills Kpeli, et al., "Engineering Dense Tumor Constructs via Cellular Contraction of Extracellular Matrix Hydrogels," *Biotechnology and Bioengineering* 121, no. 1 (2024): 380-394, https://doi.org/10.1002/bit.28561.

58. C. Raub, A. Putnam, B. Tromberg, and S. George, "Predicting Bulk Mechanical Properties of Cellularized Collagen Gels Using Multiphoton Microscopy," *Acta Biomater* 6, no. 12 (2010): 4657-4665, https://doi.org/10.1016/j.actbio.2010.07.004.

59. S. A. Kim, E. K. Lee, and H. J. Kuh, "Co-Culture of 3D Tumor Spheroids with Fibroblasts as a Model for Epithelial–Mesenchymal Transition In Vitro," *Experimental Cell Research* 335, no. 2 (2015): 187-196, https://doi.org/10.1016/j.yexcr.2015.05.016.

60. S. Nakagawa, P. Pawelek, and F. Grinnell, "Long-term Culture of Fibroblasts in Contracted Collagen Gels: Effects on Cell Growth and Biosynthetic Activity," *Journal of Investigative Dermatology* 93, no. 6 (1989): 792-798, https://doi.org/10.1111/1523-1747.ep12284425.

61. K. M. Yamada and E. Cukierman, "Modeling Tissue Morphogenesis and Cancer in 3D," *Cell* 130, no. 4 (2007): 601-610, https://doi.org/10.1016/j.cell.2007.08.006.

62. S. Xu, H. Xu, W. Wang, et al., "The Role of Collagen in Cancer: from Bench to Bedside," *Journal of Translational Medicine* 17, no. 1 (2019): 309, https://doi.org/10.1186/s12967-019-2058-1.

63. T. Chanmee, P. Ontong, and N. Itano, "Hyaluronan: a Modulator of the Tumor Microenvironment," *Cancer Letters* 375, no. 1 (2016): 20-30, https://doi.org/10.1016/j.canlet.2016.02.031.

64. L. Song, H. Qiu, Z. Chen, et al., "Injectable Hyaluronate/Collagen Hydrogel with Enhanced Safety and Efficacy for Facial Rejuvenation," *Collagen and Leather* 6, no. 1 (2024): 21, https://doi.org/10.1186/s42825-024-00165-7.

65. C. A. S. Corsa, A. Brenot, W. R. Grither, et al., "The Action of Discoidin Domain Receptor 2 in Basal Tumor Cells and Stromal Cancer-Associated Fibroblasts Is Critical for Breast Cancer Metastasis," *Cell Reports* 15, no. 11 (2016): 2510-2523, https://doi.org/10.1016/j.celrep.2016.05.033.

66. A. Hyytiäinen, K. Korelin, M. Toriseva, et al., "The Effect of Matrices on the Gene Expression Profile of Patient-derived Head and Neck Carcinoma Cells for in Vitro Therapy Testing," *Cancer Cell International* 23, no. 1 (2023): 147, https://doi.org/10.1186/s12935-023-02982-y.

67. K. Tuomainen, A. Al-Samadi, S. Potdar, et al., "Human Tumor–Derived Matrix Improves the Predictability of Head and Neck Cancer Drug Testing," *Cancers* 12, no. 1 (2020): 1, https://doi.org/10.3390/cancers12010092.

68. B. N. Mason, A. Starchenko, R. M. Williams, L. J. Bonassar, and C. A. Reinhart-King, "Tuning Three-Dimensional Collagen Matrix Stiffness Independently of Collagen Concentration Modulates Endothelial Cell Behavior," *Acta Biomaterialia* 9, no. 1 (2013): 4635-4644, https://doi.org/10.1016/j.actbio.2012.08.007.

69. J. Kanta, "Collagen Matrix as a Tool in Studying Fibroblastic Cell Behavior," *Cell Adhesion & Migration* 9, no. 4 (2015): 308-316, https://doi.org/10.1080/19336918.2015.1005469.

70. S. T. Kreger and S. L. Voytik-Harbin, "Hyaluronan Concentration Within a 3D Collagen Matrix Modulates Matrix Viscoelasticity, But Not Fibroblast Response," *Matrix Biology* 28, no. 6 (2009): 336-346, https://doi.org/10.1016/j.matbio.2009.05.001.

71. J. K. Kutty, E. Cho, J. Soo Lee, N. R. Vyavahare, and K. Webb, "The Effect of Hyaluronic Acid Incorporation on Fibroblast Spreading and Proliferation within PEG-diacrylate Based Semi-interpenetrating Networks," *Biomaterials* 28, no. 33 (2007): 4928-4938, https://doi.org/10.1016/j.biomaterials.2007.08.007.

72. M. Anguiano, X. Morales, C. Castilla, et al., "The Use of Mixed Collagen-Matrigel Matrices of Increasing Complexity Recapitulates the Biphasic Role of Cell Adhesion in Cancer Cell Migration: ECM Sensing, Remodeling and Forces at the Leading Edge of Cancer Invasion," *PLoS ONE* 15, no. 1 (2020): 0220019, https://doi.org/10.1371/journal.pone.0220019.

73. N. Sachs, J. de Ligt, O. Kopper, et al., "A Living Biobank of Breast Cancer Organoids Captures Disease Heterogeneity," *Cell* 172, no. 1-2 (2018): 373–386.e10, https://doi.org/10.1016/j.cell.2017.11.010.

74. O. M. Maria, A. Zeitouni, O. Gologan, and S. D. Tran, "Matrigel Improves Functional Properties of Primary Human Salivary Gland Cells," *Tissue Engineering Part A* 17, no. 9-10 (2011): 1229-1238, https://doi.org/10.1089/ten.TEA.2010.0297.

75. T. Jin, L. Li, R. C. Siow, and K. K. Liu, "Collagen Matrix Stiffness Influences Fibroblast Contraction Force," *Biomedical Physics & Engineering Express* 2, no. 4 (2016): 047002, https://doi.org/10.1088/2057-1976/2/4/047002.

76. G. Wollensak, E. Spoerl, F. Reber, and T. Seiler, "Keratocyte Cytotoxicity of Riboflavin/UVA-Treatment In Vitro," *Eye (Lond)* 18, no. 7 (2004): 718-722, https://doi.org/10.1038/sj.eye.6700751.

77. H. W. Sung, D. M. Huang, W. H. Chang, R. N. Huang, and J. C. Hsu, "Evaluation of Gelatin Hydrogel Crosslinked with Various Crosslinking Agents as Bioadhesives: in Vitro Study," *Journal of Biomedical Materials Research* 46, no. 4 (1999): 520-530, https://doi.org/10.1002/(SICI)1097-4636(19990915)46:4⟨520::AID-JBM10⟩3.0.CO;2-9.

78. T. Agarwal, N. Celikkin, M. Costantini, T. K. Maiti, and P. Makvandi, "Recent Advances in Chemically Defined and Tunable Hydrogel Platforms for Organoid Culture," *Bio-Design and Manufacturing* 4, no. 3 (2021): 641-674, https://doi.org/10.1007/s42242-021-00126-7.

79. K. M. Beussman, M. L. Rodriguez, A. Leonard, N. Taparia, C. R. Thompson, and N. J. Sniadecki, "Micropost Arrays for Measuring Stem Cell-derived Cardiomyocyte Contractility," *Methods* 94 (2016): 43-50, https://doi.org/10.1016/j.ymeth.2015.09.005.

80. B. J. Gill and J. L. West, "Modeling the Tumor Extracellular Matrix: Tissue Engineering Tools Repurposed towards New Frontiers in Cancer Biology," *Journal of Biomechanics* 47, no. 9 (2014): 1969-1978, https://doi.org/10.1016/j.jbiomech.2013.09.029.

81. C. Cha, E. Antoniadou, M. Lee, et al., "Tailoring Hydrogel Adhesion to Polydimethylsiloxane Substrates Using Polysaccharide Glue," *Angewandte Chemie International Edition* 52, no. 27 (2013): 6949-6952, https://doi.org/10.1002/anie.201302925.

82. S. E. Park, A. Georgescu, J. M. Oh, K. W. Kwon, and D. Huh, "Polydopamine-Based Interfacial Engineering of Extracellular Matrix Hydrogels for the Construction and Long-Term Maintenance of Living Three-Dimensional Tissues," *ACS Applied Materials & Interfaces* 11, no. 27 (2019): 23919-23925, https://doi.org/10.1021/acsami.9b07912.

83. D. Utami Nike, M. F. Ni, N. Sallehuddin, et al., "Genipin-Crosslinking Effects on Biomatrix Development for Cutaneous Wound Healing: a Concise Review," *Frontiers in Bioengineering and Biotechnology* 10 (2022), https://doi.org/10.3389/fbioe.2022.865014.

84. Y. Wu, S. Joseph, and N. R. Aluru, "Effect of Cross-Linking on the Diffusion of Water, Ions, and Small Molecules in Hydrogels," *The Journal*

of Physical Chemistry B 113, no. 11 (2009): 3512-3520, https://doi.org/10.1021/jp808145x.

85. M. J. Moura, M. H. Gil, and M. M. Figueiredo, "Delivery of Cisplatin from Thermosensitive co-cross-linked Chitosan Hydrogels," *European Polymer Journal* 49, no. 9 (2013): 2504-2510, https://doi.org/10.1016/j.eurpolymj.2013.02.032.

86. A. W. Martinez, J. M. Caves, S. Ravi, W. Li, and E. L. Chaikof, "Effects of Crosslinking on the Mechanical Properties, Drug Release and Cytocompatibility of Protein Polymers," *Acta Biomaterialia* 10, no. 1 (2014): 26-33, https://doi.org/10.1016/j.actbio.2013.08.029.

87. L. Wang, X. Li, Y. Ren, et al., "Cancer-Associated Fibroblasts Contribute to Cisplatin Resistance by Modulating ANXA 3 in Lung Cancer Cells," *Cancer Science* 110, no. 5 (2019): 1609-1620, https://doi.org/10.1111/cas.13998.

88. J. De Las Rivas, A. Brozovic, S. Izraely, A. Casas-Pais, I. P. Witz, and A. Figueroa, "Cancer Drug Resistance Induced by EMT: Novel Therapeutic Strategies," *Archives of Toxicology* 95, no. 7 (2021): 2279-2297, https://doi.org/10.1007/s00204-021-03063-7.

89. A. Brooks, Y. Zhang, J. Chen, and C. X. Zhao, "Cancer Metastasis-on-a-Chip for Modeling Metastatic Cascade and Drug Screening," *Advanced Healthcare Materials* 13, no. 21 (2024): 2302436, https://doi.org/10.1002/adhm.202302436.

90. H. Xu, J. Wen, J. Yang, et al., "Tumor-microenvironment-on-a-chip: the Construction and Application," *Cell Communication and Signaling* 22, no. 1 (2024): 515, https://doi.org/10.1186/s12964-024-01884-4.

91. C. G. Uhl and Y. Liu, "Microfluidic Device for Expedited Tumor Growth towards Drug Evaluation," *Lab Chip* 19, no. 8 (2019): 1458-1470, https://doi.org/10.1039/c8lc01250d.

92. Y. Juste-Lanas, S. Hervas-Raluy, J. M. García-Aznar, and A. González-Loyola, "Fluid Flow to Mimic Organ Function in 3D in Vitro Models," *APL Bioeng* 7, no. 3 (2023): 031501, https://doi.org/10.1063/5.0146000.

93. C. M. Leung, P. de Haan, K. Ronaldson-Bouchard, et al., "A Guide to the Organ-on-a-chip," *Nature Reviews Methods Primers* 2, no. 1 (2022): 33, https://doi.org/10.1038/s43586-022-00118-6.

94. M. Martinez and E. K. Moon, "CAR T Cells for Solid Tumors: New Strategies for Finding, Infiltrating, and Surviving in the Tumor Microenvironment," *Frontiers in Immunology* 10 (2019): 128, https://doi.org/10.3389/fimmu.2019.00128.

95. T. H. Booij, L. S. Price, and E. H. J. Danen, "3D Cell-Based Assays for Drug Screens: Challenges in Imaging, Image Analysis, and High-Content Analysis," *SLAS DISCOVERY: Advancing the Science of Drug Discovery* 24, no. 6 (2019): 615-627, https://doi.org/10.1177/2472555219830087.

96. O. Z. Kraus and B. J. Frey, "Computer Vision for High Content Screening," *Critical Reviews in Biochemistry and Molecular Biology* 51, no. 2 (2016): 102-109, https://doi.org/10.3109/10409238.2015.1135868.

Supporting Information

Additional supporting information can be found online in the Supporting Information section.

Supporting File 1: adhm71227-sup-0001-SuppMat.docx.

Supporting File 2: adhm71227-sup-0002-File_S1.dxf.

Supporting File 3: adhm71227-sup-0003-File_S2.mp4.

Supporting File 4: adhm71227-sup-0004-File_S3.avi.

Supporting File 5: adhm71227-sup-0005-Data.zip.